



Marine heatwaves in the Western North Pacific Region: Historical characteristics and future projections



Wenjin Sun^{a,b,c,d}, Lijun Yin^a, Yufei Pei^a, Chuang Shen^a, Yifei Yang^a, Jinlin Ji^{a,c}, Jingsong Yang^{b,c}, Changming Dong^{a,c,*}

^a School of Marine Sciences, Nanjing University of Information Science and Technology, Nanjing, China

^b State Key Laboratory of Satellite Ocean Environment Dynamics, Second Institute of Oceanography, Ministry of Natural Resources, Hangzhou, China

^c Southern Marine Science and Engineering Guangdong Laboratory (Zhuuhai), Zhuuhai, China

^d GEOMAR Helmholtz Centre for Ocean Research Kiel, Kiel, Germany

ARTICLE INFO

Keywords:

Marine heatwave
Historical characteristics
Future projections
Western north Pacific region
CMIP6

ABSTRACT

This study investigates the historical characteristics and future trends of marine heatwaves (MHWs) in the Western North Pacific (WNP) region. During the historical period from 1982 to 2014, the WNP region experiences an average MHW frequency of 0.89 ± 0.18 count/year. These events have an average duration of 8.64 ± 1.39 days/count. Annually, the cumulative MHW days amount to 7.76 ± 2.23 days, with an accumulated intensity of 15.73 ± 6.43 °C days. The maximum intensity recorded during this period reaches 2.04 ± 0.54 °C, while the average intensity stands at 1.74 ± 0.48 °C/count. In the evaluation of 14 CMIP6 models, five optimal models, namely GFDL-ESM4, EC-Earth3-Veg, EC-Earth3, BCC-CSM2-MR, and MRI-ESM2-0, are selected for simulating future MHWs. Based on the simulation results of these five models under the SSP2-4.5 and SSP5-8.5 scenarios for the future period (2015–2100), it is found that under the SSP2-4.5, the frequency of MHWs is slightly higher compared to the SSP5-8.5. However, under the SSP5-8.5, MHWs exhibit higher accumulated intensity, maximum intensity, and average intensity, with a predominance of high-intensity MHWs in the Kurashio Extension region. The occurrence area ratio in the future is significantly larger than in the historical period. Moreover, MHWs intensity displays a seasonal variation, with stronger during summer and weaker during winter. This study provides important insights into MHWs in the WNP region, offering valuable information for decision-makers in formulating response measures and reducing economic losses.

1. Introduction

Marine heatwaves (MHWs) occur when sea surface temperatures (SST) persistently exceed a specific threshold for an extended period of time (Pearce and Feng, 2013). In recent decades, MHWs show an increasing trend in frequency, duration, spatial extent, and intensity (Frölicher et al., 2018). From 1925 to 2016, the global annual average frequency of MHWs increases by 34%, and their duration increases by 17% (Oliver et al., 2018). These increasing trends align with observed changes in SST, suggesting that global warming will lead to more frequent and longer-lasting MHWs. Simulations conducted using global climate models indicate a significant increase in the intensity and annual duration of MHWs throughout the 21st century as well (Oliver et al., 2019; Hayashida et al., 2020; Plecha and Soares, 2020). This inference is also supported by other studies (Sun et al., 2022a; Wang et al., 2023a).

MHWs continue to have severe consequences for marine ecosystems, including the widespread death of marine organisms and coral bleaching (Wernberg et al., 2013; Laufkötter et al., 2020; Oliver et al., 2020; Smith et al., 2021, 2023; Szymkowiak and Steinkruger, 2023). For instance, an MHW in Western Australia in 2011 had significant effects on the survival of local scallops, crabs, and fisheries, resulting in a large-scale mortality of abalone (Chandrapavan et al., 2019). In the Mediterranean region, MHWs during the period from 2015 to 2019 led to mass mortality of local marine organisms (Garrabou et al., 2022). The record-breaking MHW event that occurs in the Great Barrier Reef in 2016, which leads to extensive coral mortality, coral bleaching, and impacts on surface zooplankton communities (Le et al., 2022; Noh et al., 2022; Arteaga et al., 2023). This event further exacerbates the spread of potential pathogens on the reef, posing a significant threat to marine biodiversity in this region (Doni et al., 2023). Overall, MHWs have detrimental

* Corresponding author. School of Marine Sciences, Nanjing University of Information Science and Technology, Nanjing, China.
E-mail address: cmdong@nuist.edu.cn (C. Dong).

effects on marine ecosystems, genetic diversity, biodiversity, fisheries, and aquaculture (Mills et al., 2013; Cavole et al., 2016; Plecha et al., 2021; Yao and Wang, 2022).

The generation mechanisms of MHWs are complex and diverse (Holbrook et al., 2019; Sen et al., 2020), and they can be classified into three types based on their sources of heat. The first type consists of MHWs primarily influenced by atmospheric forcing (Rodrigues et al., 2019; Gao et al., 2020; Oh et al., 2023; Li et al., 2023). For instance, the MHWs in the Northeast Pacific during the winter of 2013–2014 are caused by anomalous high-pressure systems (Capotondi et al., 2022; Chen et al., 2023). Record-breaking MHWs in the winter of 2019–2020 in the Northeast Pacific and in 2020 in the Northwest Pacific are attributed to anomalies in the sea surface heat fluxes (Chen et al., 2021; Yao et al., 2023). The second type of MHWs is primarily driven by oceanic factors (Elzahaby et al., 2021). Such as, the occurrence and variability of MHWs in the Gulf of Alaska from 2012 to 2015 are closely related to historical changes in large-scale SST in the Kuroshio Extension (KE) region. Oceanic circulation anomalies are responsible for MHWs in the Tasman Sea in 2015–2016 (Oliver et al., 2017) and in the Mid-Atlantic Bight in 2017 (Gawarkiewicz et al., 2019). The third type of MHWs occurs as a result of the combined influence of atmospheric and oceanic factors (Benthuysen et al., 2014). Recent research indicates that MHWs on the northern continental shelf of the South China Sea (SCS) are jointly influenced by air-sea heat fluxes and oceanic advection, associated with anticyclonic anomalies over the Northwest Pacific and the El Niño phenomenon (Yao and Wang, 2021; Wang et al., 2022a, 2023b; Liu et al., 2022).

The Western North Pacific (WNP) region experiences significant influence from monsoons, resulting in high temperatures and increasing water temperatures during the summer. These meteorological and climatic conditions create favorable conditions for the occurrence of MHWs in this area (Wang et al., 2022b). Yang et al. (2022) conducts a detailed study on the characteristics of historical period MHWs in this region based on OISSTV2 and CMIP6 data. However, their study defines MHWs using a 90th percentile threshold and a fixed climatological baseline, without accounting for the impacts of global warming. As a result, the MHWs in the future period become exceptionally intense and frequent, with some cases of continuous MHWs conditions throughout the year, deviating from the concept of MHWs as a catastrophic event. This study further investigates it using a method based on the 95th percentile and a 20-year sliding climatological threshold. Detailed comparisons are made between the results of this study and those of Yang et al. (2022). Given the frequent and severe occurrence of MHWs in this region, this study enriches our understanding of MHWs in the WNP area, offering a more comprehensive reference for the development of future MHW forecasting systems.

The study is structured as follows. In the second section, we begin by introducing the OISSTV2 dataset, which is utilized for identifying MHWs, as well as the CMIP6 dataset. Subsequently, we discuss the methodology employed for defining MHWs and explain the scoring method used for selecting the preferred CMIP6 models. Moving on to the third section, we present the key research findings of this study. This includes an analysis of the historical characteristics of MHWs in the WNP region, as well as projections regarding the future evolution of MHWs based on the selected CMIP6 model data. In the fourth section, we delve into the annual SST variance and the spatial distribution of thresholds under different scenarios. This exploration aims to uncover the underlying mechanisms behind the distinctions in MHW characteristics between the KE and other regions. Finally, in the last section, we summarize the primary conclusions drawn from the study and explore potential avenues for future research.

2. Data and methods

2.1. OISSTV2 data

The SST data used in this study are sourced from the Optimum Interpolation Sea Surface Temperature Version 2 (OISSTV2) dataset, which is provided by the National Oceanic and Atmospheric Administration (NOAA) in the United States. The dataset has a spatial resolution of $0.25^\circ \times 0.25^\circ$ and a daily temporal resolution. OISSTV2 combines and interpolates data from various observation sources, including satellites, ships, and buoys. It undergoes rigorous bias adjustments using in-situ data to ensure its accuracy and reliability (Reynolds et al., 2007).

For this study, we employ the OISSTV2 dataset covering the WNP region ($100^\circ\text{E} \sim 180^\circ\text{E}$, $0\text{--}65^\circ\text{N}$) from 1982 to 2014. The OISSTV2 dataset has been extensively utilized in research on MHWs in various regions worldwide, highlighting its suitability for such studies (Oliver et al., 2017, 2018; Yan et al., 2020; Belyiana et al., 2022; Jacox et al., 2022; Zhang et al., 2022). Further details and specifics regarding the OISSTV2 dataset can be found in Reynolds et al. (2007).

2.2. CMIP6 data

The Coupled Model Intercomparison Project (CMIP) is an ongoing effort led by the World Climate Research Programme (WCRP) to evaluate and compare global climate models. It began in 1995 and has undergone multiple phases of development. The current phase, CMIP6, aims to enhance our understanding of climate change by providing improved climate model simulations and projections (Eyring et al., 2016; O'Neill et al., 2016; Qiu et al., 2021; Wei et al., 2021; Scafetta, 2022). CMIP6 introduces new scenarios known as Shared Socioeconomic Pathways (SSPs), which incorporate different socioeconomic assumptions and represent diverse potential futures. In this study, we utilize two types of SSPs from CMIP6's Scenario Model Intercomparison Project (Scenario MIP): SSP2-4.5 and SSP5-8.5.

SSP2-4.5 corresponds to a medium emissions scenario where it is projected that radiative forcing will remain below 4.5 W/m^2 by the year 2100. In contrast, SSP5-8.5 represents a high emissions scenario, with radiative forcing projected to reach 8.5 W/m^2 by 2100. The analysis covers both the historical period from 1982 to 2014 and the future period from 2015 to 2100. To assess the performance of CMIP6 models in simulating MHWs, we compare the historical characteristics of MHWs with data obtained from the OISSTV2 dataset. A total of 14 model sets are chosen from the "r1i1p1f1" simulation scenario. These selections adhere to specific criteria, requiring data availability for both historical and future projection scenarios (SSP1-2.6, SSP2-4.5, SSP3-7.0, and SSP5-8.5). Additionally, the selected models possess a resolution higher than 250 km. A comprehensive breakdown of these model selections is outlined in Table 1. To facilitate the comparison, all data are interpolated to a grid resolution of $1^\circ \times 1^\circ$ before conducting the analysis.

2.3. Methodology for marine heatwaves detection

Currently, various methods are proposed for defining MHWs. The most commonly used method, introduced by Hobday et al. (2016), defines a threshold for identifying MHWs as the 90th percentile of SST during a climatological reference baseline. An MHW is defined as an event in which the SST remains above the threshold for at least five consecutive days with no more than a 2-day interval. The selection of a climatological reference baseline can be categorized into two types: fixed reference period and sliding climatological reference period (Liu et al., 2014; Jacox et al., 2019). In studies of MHWs using satellite observation data, researchers commonly adopt a fixed climatological period to establish the threshold baseline. This approach is primarily driven by the limited availability of observational data, which typically covers the time period from 1982 to the present. Given this constraint, the selection of the climatological reference baseline has minimal

Table 1

Basic information of 14 models from CMIP6.

Number	Model Name	Institution (Country or Region)	Spatial Resolution (km)	Oceanic Grid (lon x lat)
1	AWI-CM-1-1-MR	AWI (Germany)	25	Unstructured grid
2	BCC-CSM2-MR	BCC (China)	100	360 × 232
3	CanESM5	CCCma (Canada)	100	360 × 291
4	CESM2-WACCM	NCAR (America)	100	384 × 320
5	CMCC-CM2-SR5	CCMC (Italy)	100	362 × 292
6	CMCC-ESM2	CCMC (Italy)	100	362 × 292
7	EC-Earth3	EC (Europe)	100	362 × 292
8	EC-Earth3-Veg	EC (Europe)	100	362 × 292
9	EC-Earth3-Veg-LR	EC (Europe)	100	362 × 292
10	GFDL-ESM4	NOAA-GFDL (America)	50	720 × 576
11	IPSL-CM6A-LR	IPSL (France)	100	362 × 332
12	MIROC6	MIROC (Japan)	100	360 × 256
13	MPI-ESM1-2-HR	MPI-M (Germany)	50	802 × 404
14	MRI-ESM2-0	MRI (Japan)	100	360 × 180

influence on the study results. However, when using numerical models to predict future MHW characteristics, a fixed climatological reference baseline can lead to an overestimation of MHW frequency and intensity in the future. This is because the fixed baseline cannot remove the global warming effect, resulting in an unrealistic scenario where MHWs become very frequent in the future, and certain regions may experience MHWs throughout the year (Chiswell, 2022).

In this study, we modify the approach used by Hobday et al. (2016) by setting the threshold as the 95th percentile of SST during the climatological reference period. This modification enables us to specifically target MHWs that exhibit higher intensity and have a more significant impact. Additionally, in contrast to the fixed climatological reference period employed by Yang et al. (2022), we have adopted the approach recommended by Chiswell (2022) and Kajtar et al. (2022), which involves using a 20-year sliding window for the climatological baseline. This approach enables us to account for changing climate trends and capture the potential intensification of MHWs.

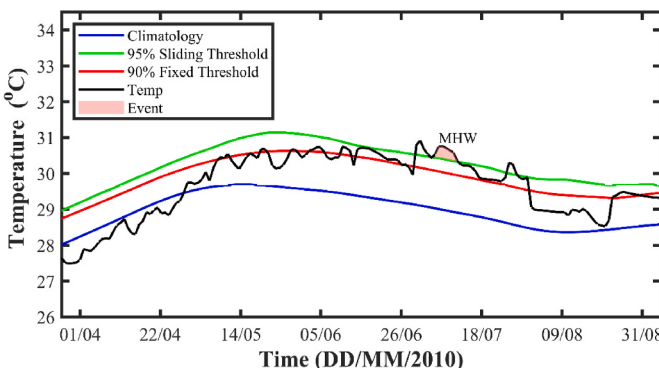


Fig. 1. Example of a marine heatwave case. The blue curve represents the climatological SST average, the green curve represents the temperature threshold baseline of the 95th percentile during the sliding climatological reference period (1995–2014), the red curve represents the temperature threshold baseline of the 90th percentile during the fixed climatological reference period (1982–2014), the black line represents the observational SST, and the red shaded region indicates a marine heatwave event.

Fig. 1 illustrates the identification of an MHW at a specific location (115°E, 12°N) in the WNP region. The black curve represents the SST observed during the given period in the OISSTV2 dataset, while the blue curve represents the threshold baseline corresponding to the 95th percentile of the climatological reference period (1995–2014). The red curve corresponds to the threshold baseline of the 90th percentile from the fixed climatological reference period (1982–2014) as utilized in Yang et al. (2022). The red shading indicates the occurrence of the MHW, which took place from July 6, 2010, to July 12, 2010, with an average intensity of 1.77 °C. It is worth noting that there are two instances of SST exceeding the threshold baseline before and after this MHW event. However, due to their short duration, they are not being identified as MHWs. Furthermore, as evident from the figure, adopting the definition from Yang et al. (2022) results in longer durations for the identified MHWs compared to the definition employed in this study. Hence, the divergence in MHW definitions significantly influences the characteristics of them.

2.4. CMIP6 evaluation method

To evaluate the performance of the selected CMIP6 models in capturing historical MHWs, this study compares six parameters derived from the OISSTV2 dataset with those obtained from the CMIP6 model data. These parameters include the frequency, duration, annual cumulative days (Days), cumulative intensity (CumInt), maximum intensity (MaxInt), and mean intensity (MeanInt) of MHWs. This study uses two evaluation metrics, the spatial skill metric (M1) and the Taylor score (TS), to assess the simulation performance of the models regarding the characteristics of MHWs.

The expression for spatial skill metric is as follows:

$$M1 = 1 - \frac{MSE(C, O)}{MSE(\bar{O}, O)} \quad (1)$$

The mean square error (MSE) is defined as:

$$MSE(C, O) = \frac{1}{N} \sum_{i=1}^N \gamma_i (C_i - O_i)^2 \quad (2)$$

where N represents the total grid points, and γ_i represents the weighting assigned to each grid point, determined by the ratio of the actual distance along the longitude (0.5° on each side) to the actual distance along the latitude (0.5° on each side) for each grid point. C_i and O_i represent a specific feature of MHWs for the CMIP6 and OISSTV2 models, respectively, at a given point during the historical period. The overline denotes spatial averaging in the WNP region. The closer the $M1$ value is to 1, the more accurate the model simulation of MHW characteristics (Chen et al., 2011).

The calculation formula for the Taylor Score is as follows:

$$TS = \frac{4(1+R)^4}{\left(\frac{\sigma_c}{\sigma_0} + \frac{\sigma_0}{\sigma_c}\right)^2 (1+R_0)^4} \quad (3)$$

where R represents the correlation coefficient of the MHWs detection results between CMIP6 models and OISSTV2 data. R_0 is the theoretical maximum value of the correlation coefficient, set to 1.0 in this study. σ_c and σ_0 represent the standard deviations of the spatial distribution of MHWs characteristics for CMIP6 and OISSTV2, respectively. A higher Taylor Score indicates a better agreement between the CMIP6 model results and OISSTV2 data in terms of the MHWs (Taylor, 2001).

The scores for each parameter (M1 and TS) of the models for the six MHW parameters are projected onto a score range of 20–100 using the following calculation formula:

$$S_{k,i} = \frac{f_{k,\max} - f_{k,i}}{f_{k,\max} - f_{k,\min}} \times 80 + 20, k = 1, 2, 3, \dots, 12, \quad i = 1, 2, 3, \dots, 14 \quad (4)$$

The score ($S_{k,i}$) for a specific MHW parameter (e.g., MHW frequency) based on a particular evaluation index (e.g., M1). $f_{k,i}$, $f_{k,\min}$, and $f_{k,\max}$ represent the raw score of a certain evaluation index for a specific model, as well as the minimum and maximum scores among the 14 models, respectively. After the transformation described in Equation (4), the scores for each index of the simulated values of each MHW parameter are scaled between 20 and 100. This approach helps mitigate the impact of exceptionally low or high scores for a particular MHW parameter due to the model's performance. Finally, the average scores of the six MHW feature parameters are calculated with equal weights, and the models are ranked based on these average scores. The top five models (GFDL-ESM4, EC-Earth3-Veg, EC-Earth3, BCC-CSM2-MR, and MRI-ESM2-0, Fig. 2) with the highest scores are selected for future projections and analysis of MHWs.

3. Results

3.1. Marine heatwave characteristics during the historical period

The spatial distribution of MHW frequency in the WNP region during the historical period (1982–2014) is depicted in Fig. 3a. Here, MHW frequency is defined as the average number of MHW occurrences in one year. Its distribution shows distinct bands of varying frequencies. Higher MHW frequencies are observed near Hainan Island, east of Taiwan Island with the northwestern Pacific subtropical countercurrent, and north of the KE region. The average frequency of MHWs in the WNP region is 0.89 ± 0.18 count/year, which is less than half of the findings (1.95 ± 0.21 count/year) reported in Yang et al. (2022). The highest frequency, reaching 1.52 count/year, is found in the north of the KE region at (152°E, 44°N), while the lowest frequency, with only 0.36 count/year, occurs near the equatorial position at (141°E, 0).

The duration of MHWs represents the length of a single MHW event persists. In contrast to the spatial distribution of MHW frequency depicted in Fig. 3a, the regions with higher MHW durations are mainly situated in the north part of the WNP region (Fig. 3b). Conversely, the

low-latitude regions and marginal seas tend to exhibit shorter MHW durations. The average duration in the WNP region is 8.64 ± 1.39 days/count, which is slightly lower than the findings (11.38 ± 1.97 days/count) reported in Yang et al. (2022). The maximum duration of 14.56 days is observed in the offshore area downstream of the KE region at (176°E, 40°N), while the minimum duration of 5.65 days/count is found in the low-latitude region at (152°E, 3°N).

The annual cumulative days of MHWs represents the total duration of multiple MHWs over one year. It is determined by multiplying the MHW frequency (Fig. 3a) and the duration of MHWs (Fig. 3b). The most prominent feature is the high-value distribution in the KE region and its northern open sea area (Fig. 3c). On average, the WNP region experiences 7.76 ± 2.23 days/year of accumulated MHWs, which is approximately one-third of the findings (22.06 ± 3.84 days/year) reported in Yang et al. (2022). The maximum value of 15.85 days/year is observed in the north of the KE region at (178°E, 43°N), while the minimum value of 2.21 days/year, similar to the frequency (Fig. 3a), is found in the equatorial area at (141°E, 0).

Accumulated intensity represents cumulative heat content associated with MHWs, calculated by multiplying MHW intensity by the event duration. It represents the physical significance of the total heat anomaly generated during a single MHW event. The average values is 15.73 ± 6.43 °C days, which is slightly lower than the findings (18.06 ± 7.67 °C days) presented in Yang et al. (2022); However, the disparity is not significant.

Maximum intensity refers to the highest SST anomaly observed during an MHW event. It represents the extreme temperature anomaly during a single event and describes the intensity during the peak phase of MHWs. The average value is 2.04 ± 0.54 °C, which is slightly higher than the findings (1.84 ± 0.50 °C) in Yang et al. (2022). This suggests that using a 20-year sliding climatological baseline yields lower climatological values compared to the fixed threshold approach used in Yang et al. (2022), thereby increasing the maximum intensity of MHWs.

Average intensity represents the average SST anomaly observed during MHWs. This represents the average impact level of an MHW

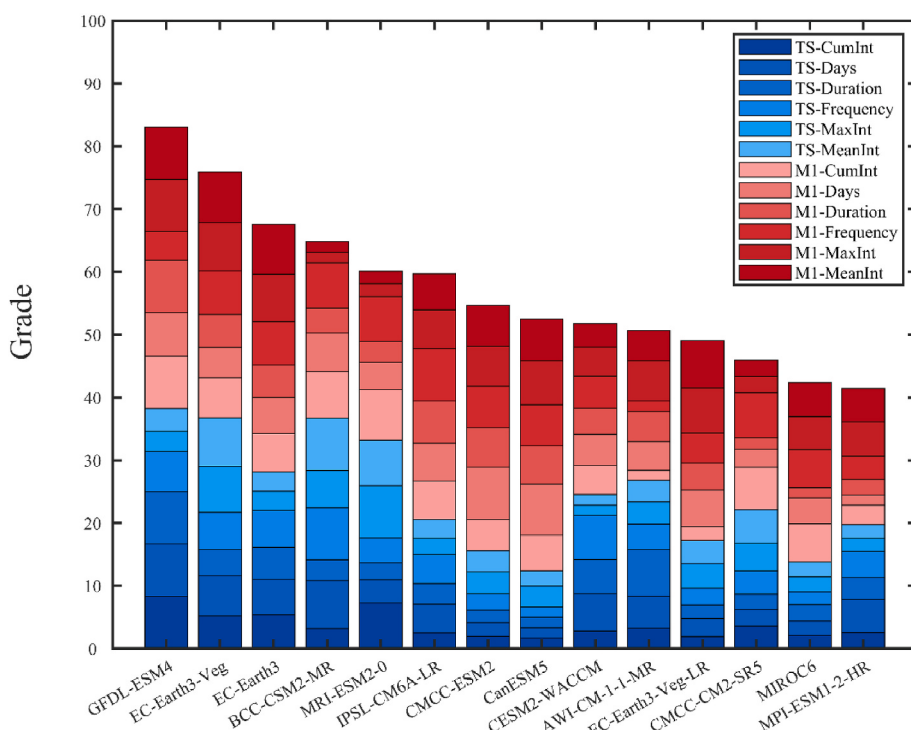


Fig. 2. Evaluation scores of 14 CMIP6 models for simulating the characteristics of MHWs in the WNP region during the historical period (1982–2014). The 12 colored blocks from bottom to top correspond to the each evaluation metrics: TS-CumInt, TS-Days, TS-Duration, TS-Frequency, TS-MaxInt, TS-MeanInt, M1-CumInt, M1-Days, M1-Duration, M1-Frequency, M1-MaxInt, M1-MeanInt.

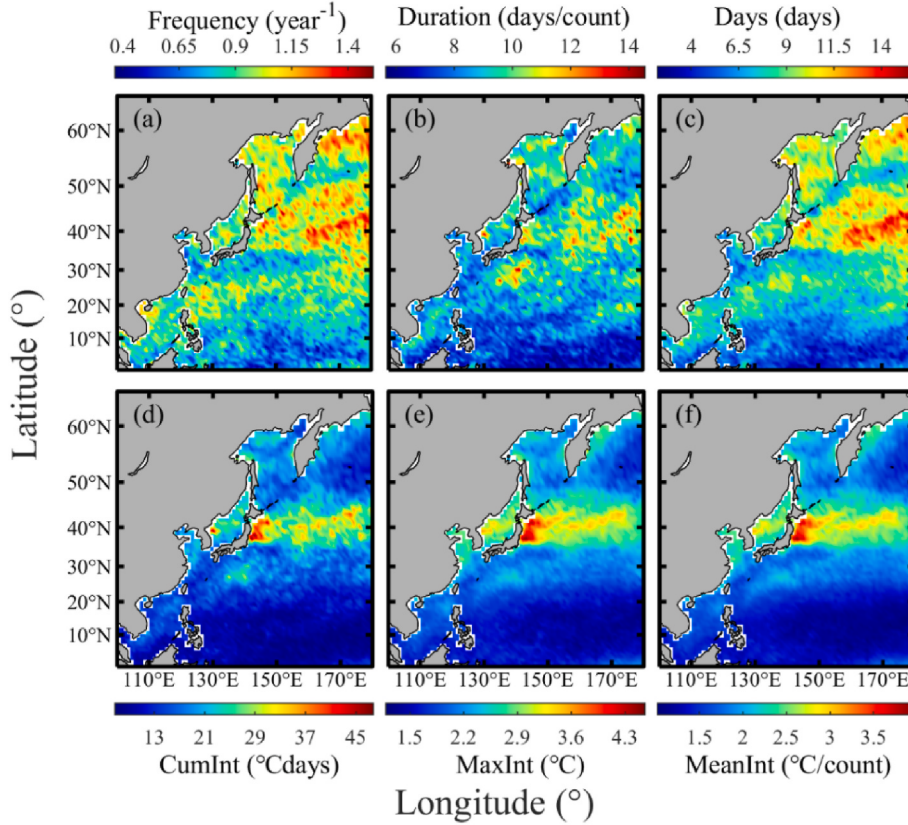


Fig. 3. Spatial distribution of the multi-year averaged MHWs characteristic in the WNP region based on OISSTV2 data. (a ~ f) represent the multi-year averaged MHWs frequency (unit: count/year), duration (unit: days/count), annual cumulative days (Days, unit: days), cumulative intensity (CumInt, unit: $^{\circ}\text{C}$ days), maximum intensity (MaxInt, unit: $^{\circ}\text{C}$), and mean intensity (MeanInt, unit: $^{\circ}\text{C}/\text{count}$), respectively.

event. The average value across the entire WNP region is 1.74 ± 0.48 $^{\circ}\text{C}/\text{count}$, which, similar to the maximum intensity, is slightly higher than the results (1.49 ± 0.42 $^{\circ}\text{C}/\text{count}$) obtained in Yang et al. (2022). The spatial distribution of accumulated intensity, maximum intensity, and average intensity of MHWs shows a consistent pattern, characterized by prominent high-value zones in the region encompassing the KE and its northern area. Particularly, the coastal areas off the eastern coast of Japan exhibit strong intensities.

Fig. 4 presents the spatial distribution of the annual trends in six characteristics of MHWs during the study period. In most of the WNP region, there is an increasing trend in the occurrence frequency (Fig. 4a). The average annual variation rate of MHW frequency is 0.26 ± 0.16 count/decade, which is approximately one-third of the findings (0.8 ± 0.4 count/decade) reported in Yang et al. (2022). The highest value of 0.91 count/decade is observed in the north of the KE region at ($154^{\circ}\text{E}, 42^{\circ}\text{N}$). However, there are also regions where the occurrence frequency has decreased. The fastest decrease rate of -0.26 count/decade is observed at ($109^{\circ}\text{E}, 0$). The spatial distribution of MHW frequency (Fig. 3a) and its trend (Fig. 4a) exhibit similar patterns. Based on the data from 1982 to 2014, it can be observed that in regions where MHWs are frequent, the frequency of MHWs is increasing over time. On the other hand, in regions where MHWs are infrequent, the frequency of MHWs is decreasing.

The average duration of MHWs shows an increasing trend over time during the historical period as well (Fig. 4b). Its distribution across the entire WNP region is relatively uniform, without any pronounced high-value areas as reported in Yang et al. (2022). The average trend in MHW duration is 0.45 ± 1.14 days/decade, with a maximum value of 7.24 days/decade observed in the north of the KE region at ($154^{\circ}\text{E}, 42^{\circ}\text{N}$). The minimum value is -6.79 days/decade, also observed in the KE region at ($156^{\circ}\text{E}, 36^{\circ}\text{N}$). The average value of the trend in duration of

MHWs is approximately one-third of the results reported in Yang et al. (2022), similar to the findings in the trend of frequency.

Significant trends in MHWs cumulative days are observed in several areas, including the region of the North Pacific Subtropical Counter-current and its southern side between the Philippines and the Hawaiian Islands, the northern KE region east of 150°E , and the Sea of Japan (Fig. 4c). The average trend in the duration of MHWs is approximately one-fifth of the results (11.7 ± 5.0 days/decade) reported in Yang et al. (2022), with a value of 2.60 ± 1.62 days/decade. The maximum value of 9.62 days/decade is observed in the north of the KE region at ($160^{\circ}\text{E}, 42^{\circ}\text{N}$). The minimum trend in MHWs cumulative days is -1.85 days/decade, observed in the north of the KE region at ($148^{\circ}\text{E}, 41^{\circ}\text{N}$).

The average annual trend of accumulated intensity, maximum intensity, and mean intensity of MHWs during the historical period are 0.67 ± 2.88 $^{\circ}\text{C}$ days/decade, -0.02 ± 0.18 $^{\circ}\text{C}/\text{decade}$, and -0.02 ± 0.14 $^{\circ}\text{C}/\text{decade}$, respectively. The location with the highest cumulative intensity is located at ($138^{\circ}\text{E}, 54^{\circ}\text{N}$), with a value of 32.20 $^{\circ}\text{C}$ days/decade. For the highest trend in maximum intensity, it is observed at ($143^{\circ}\text{E}, 54^{\circ}\text{N}$) with a value of 1.40 $^{\circ}\text{C}/\text{decade}$, and the highest trend in mean intensity is found at ($138^{\circ}\text{E}, 54^{\circ}\text{N}$) with a value of 1.10 $^{\circ}\text{C}/\text{decade}$.

The temporal trends of MHWs' frequency, duration, annual cumulative days, and cumulative intensity in the WNP region, calculated by spatially-weighted averaging over the area, reveal significant increasing trends (Fig. 5). The trends for the rates of increase in various MHW characteristics are as follows: the frequency exhibits a modest increase of 0.06 ± 0.06 count/decade (Fig. 5a), the duration shows a more pronounced increase of 0.39 ± 0.15 days/decade (Fig. 5b), the annual cumulative days demonstrate a substantial increase of 1.31 ± 0.83 days/decade (Fig. 5c), and the cumulative intensity displays a notable increase of 0.73 ± 0.55 $^{\circ}\text{C}$ days/decade (Fig. 5d). These four values are consistently much smaller than the results from Yang et al. (2022),

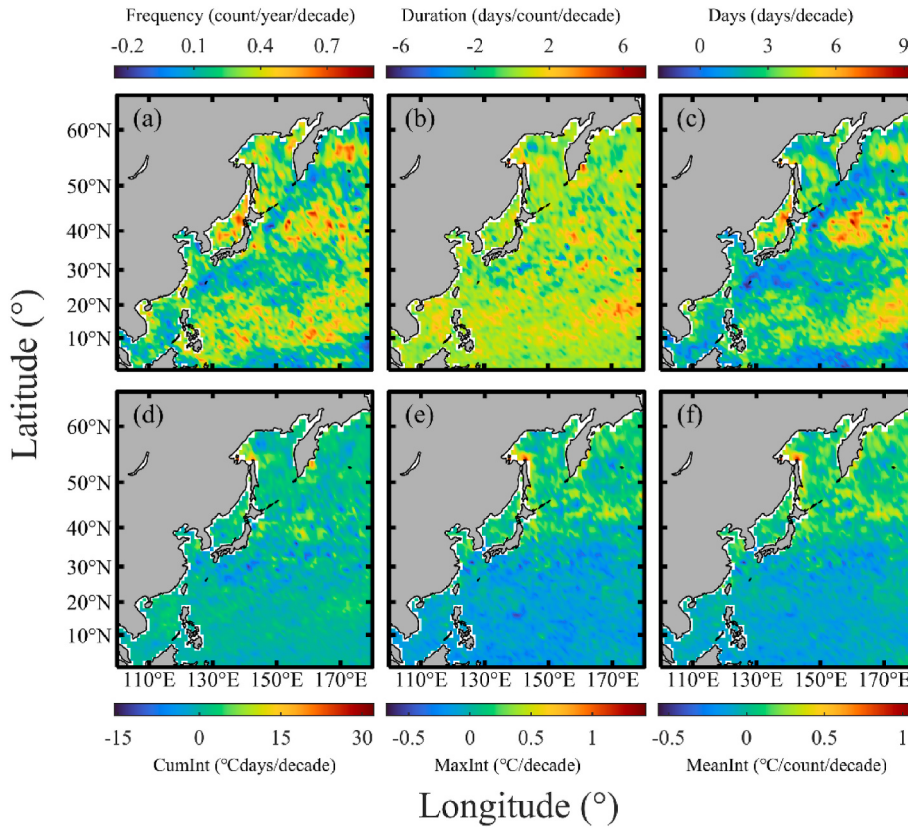


Fig. 4. Spatial distribution of multi-year averaged trends in historical MHWs features based on OISSTV2 data. (a ~ f) represent the trends in MHWs features, including frequency trend (unit: count/year/decade), duration trend (unit: days/count/decade), annual cumulative days trend (unit: days/decade), cumulative intensity trend (unit: $^{\circ}\text{C}$ days/decade), maximum intensity trend (unit: $^{\circ}\text{C}/\text{decade}$), and mean intensity trend (unit: $^{\circ}\text{C}/\text{event}/\text{decade}$).

indicating that the use of a 20-year sliding threshold method can significantly weaken the temporal trends of MHWs in the historical period. The maximum intensity and mean intensity exhibit a slight decreasing trend, with decrease rates of $-0.01 \pm 0.04 ^{\circ}\text{C}/\text{decade}$ (Fig. 5e) and $-0.01 \pm 0.03 ^{\circ}\text{C}/\text{decade}$ (Fig. 5f), respectively. Although the sign of the values indicates a decreasing trend for these two variables, the magnitudes of the changes suggest that the variability is minimal. Similar to the findings in Yang et al. (2022), the trends in these two variables can be considered negligible.

Among the six characteristic parameters of MHWs in the WNP region, only the maximum value of MHWs duration occurred in 2011 (8.59 days/conut), based on the overall average values. For the other five parameters, their maximum values all occur in 1998. Specifically, the maximum value of frequency is 2.94 count/year, annual accumulated days is 28.95 days/year, cumulative intensity is 16.90 $^{\circ}\text{C}$ days, maximum intensity is $1.97 ^{\circ}\text{C}$, and mean intensity is $1.66 ^{\circ}\text{C}/\text{count}$. This occurrence may be attributed to the strong El Niño event in 1997/98, which is an interesting phenomenon that warrants further investigation. However, this study focuses on the general trends and patterns of MHW characteristics, and a more detailed analysis of the specific event will be conducted in future research.

3.2. Marine heatwave characteristics during the future period

In this subsection, we assess the future projections of MHW characteristics based on a selected ensemble of five models under SSP2-4.5 and SSP5-8.5 scenarios. Besides, we compare our results with those of Yang et al. (2022) to illustrate the influence of using different methods for defining various characteristics of MHWs. Fig. 6a presents the spatial distribution of the average of MHWs frequency from 2015 to 2100 under the SSP2-4.5 scenario. One prominent feature is the significant

north-south asymmetry in the value of MHWs frequency. The southern region of the WNP region exhibits notably higher frequencies compared to the northern region, with the dividing line located in the KE region between 30°N and 40°N . The spatially averaged annual frequency of MHWs is 0.93 ± 0.14 count/year, slightly higher than in the historical period, but only about one-third of Yang et al. (2022). Besides, the region with the highest MHW frequency has shifted from the northern part of the KE region in the historical period to near Hainan Island at $(107^{\circ}\text{E}, 17^{\circ}\text{N})$, with a frequency of 1.31 count/year, slightly lower than the historical value of 1.52 count/year. The lowest frequency region is located at $(121^{\circ}\text{E}, 40^{\circ}\text{N})$, with a value of 0.52 count/year.

In the future period, the regions with high values of MHW duration are predominantly concentrated in the open oceans north of the KE region, as shown in Fig. 6b. This spatial distribution differs significantly from the historical period (Fig. 3b). The average value of MHWs duration is 13.63 ± 1.89 days/count, which is higher than the historical period (8.64 ± 1.39 days/count), but significantly lower than the value (86.83 ± 1.39 days/count) in Yang et al. (2022). The maximum value is 22.68 days/count observed in the northern of the KE region at $(143^{\circ}\text{E}, 42^{\circ}\text{N})$, while the minimum value is 7.98 days/count observed at $(122^{\circ}\text{E}, 6^{\circ}\text{N})$. All three values are significantly higher than their respective counterparts in the historical period.

The areas with high values of annual cumulative days are predominantly located in the open waters north of the KE (due to longer MHW durations), the southern part of the SCS, and the open oceans east of the Philippines (mainly influenced by MHW frequency) as shown in Fig. 6c. The average annual cumulative duration is 12.23 ± 1.28 days/year, surpassing the historical period's level (7.76 ± 2.23 days/year), yet considerably lower than the values (236.50 ± 29.28 days/year) reported by Yang et al. (2022). It is evident that under the MHW definition criteria used in this study, the future period's MHW cumulative days is

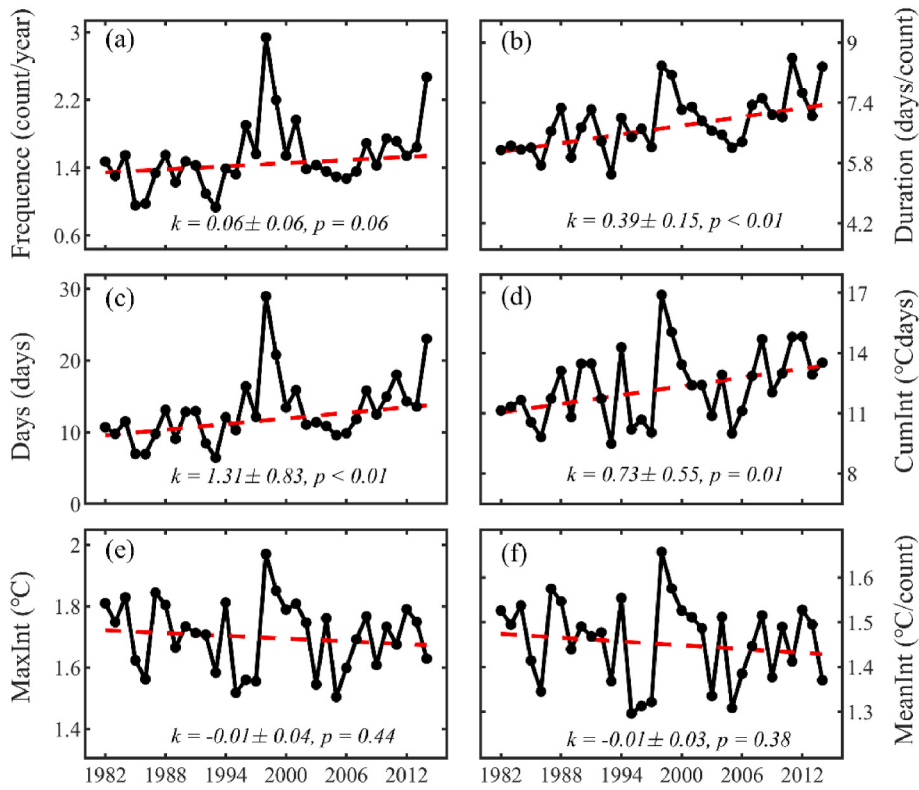


Fig. 5. Spatially-weighted average historical trends of MHWs characteristics in the WNP region based on OISSTV2 data. (a ~ f) represent the multi-year averaged MHWs frequency (unit: count/year), duration (unit: days/count), annual cumulative days (Days, unit: days/year), cumulative intensity (CumInt, unit: $^{\circ}\text{C days}$), maximum intensity (MaxInt, unit: $^{\circ}\text{C}$), and mean intensity (MeanInt, unit: $^{\circ}\text{C}/\text{count}$), respectively.

significantly shorter compared to what was indicated in Yang et al. (2022). The maximum value of 17.79 days/year occurs near the equatorial region at (119°E, 1°N), while the minimum value of 6.31 days/year is observed in the KE area at (121°E, 37°N). However, these values are higher than their corresponding counterparts in the historical period which shown in Fig. 3c.

The average value of MHWs cumulative intensity (20.85 ± 9.27 °C days, Fig. 6d) remains higher than that in the historical period (15.73 ± 6.43 °C days), but it is much lower than the value of 174.44 ± 92.62 °C days reported in Yang et al. (2022). The maximum value of 80.14 °C days occurs near the KE area at (145°E, 41°N), while the minimum value of 6.35 °C days is observed at (128°E, 40°N).

The spatially averaged maximum intensity of MHWs in the WNP region is 1.72 ± 0.60 °C, which is not only lower than observed in the historical period (2.04 ± 0.54 °C), but also weaker than the value of 2.34 ± 0.76 °C reported in Yang et al. (2022). Its highest value of 5.00 °C occurring at (139°E, 54°N), and the lowest value of 0.65 °C appearing at (120°E, 0). The spatially averaged intensity of MHWs in the WNP region is 1.50 ± 0.52 °C/count, which, similar to the maximum MHWs intensity, is lower than the values in the historical period (1.74 ± 0.48 °C/count) and the results (1.66 ± 0.53 °C/count) in Yang et al. (2022). The peak value of 4.27 °C/count is observed at (139°E, 54°N), while the minimum value of 0.56 °C/count is recorded at (120°E, 0).

The main reason for the lower values of MHW intensity (includes cumulative intensity, maximum intensity and averaged intensity) obtained in this study compared to those in Yang et al. (2022) is the higher threshold used to define MHWs, which results in weaker MHW intensities. These three characteristics exhibit a distinct zonal distribution pattern with high values in the KE region. This pattern may be attributed to the active mesoscale processes and strong ocean-atmosphere interactions in this area (Liu et al., 2012; Sun et al., 2022b). The specific mechanisms underlying this pattern are provided in the Discussion section of this study.

This study also examines the future trend in the six characteristics of MHWs during the period from 2015 to 2100. In the SSP2-4.5 scenario, the trend of MHWs frequency generally increases (Fig. 7a). Its average value is 0.04 ± 0.02 count/year/decade, maintaining a slight increasing trend, which is about one-tenth of the historical period (0.26 ± 0.16 count/year/decade). However, the results from Yang et al. (2022) indicate that the frequency of MHWs gradually decreases at a rate of -0.3 ± 0.1 count/year/decade. The occurrence of MHWs exhibits a significant upward trend near the equatorial region at (152°E, 2°N), with a maximum value of 0.13 count/year/decade. Conversely, there is a slight downward trend, indicated by a minimum value of -0.05 count/year/decade at (125°E, 9°N).

The average trend in MHWs duration is 0.19 ± 0.37 days/count/decade, as shown in Fig. 7b. This value is lower than the corresponding value in the historical period (0.45 ± 1.14 days/count/decade) and significantly lower than the value of 16.2 ± 4.4 days/count/decade indicated by Yang et al. (2022). The maximum recorded value is 2.32 days/count/decade, occurring in the vicinity of the equatorial region at (119°E, 1°N). The minimum value is -2.94 days/count/decade, occurring in the vicinity of the KE region at (143°E, 42°N).

Similarly, the average trend in the accumulated days of MHWs in the future period is 0.75 ± 0.02 days/decade (Fig. 7c). This value is lower than the corresponding value in the historical period (2.60 ± 1.62 days/decade) and significantly lower than the value of 28.5 ± 2.8 days/decade indicated by Yang et al. (2022). The maximum recorded value is 1.55 days/decade, occurring at (122°E, 31°N). The minimum value is -0.46 days/decade, occurring in the KE region at (137°E, 37°N).

In the SSP2-4.5 scenario, the average trend in the cumulative intensity is 0.32 ± 0.78 °C days/decade (Fig. 7d). Consistently with the mentioned characteristics of MHWs' duration and annual cumulative days, this value is lower than the corresponding value in the historical period (0.67 ± 2.88 °C days/decade) and also lower than the value of 38.3 ± 14.3 °C days/decade indicated by Yang et al. (2022).

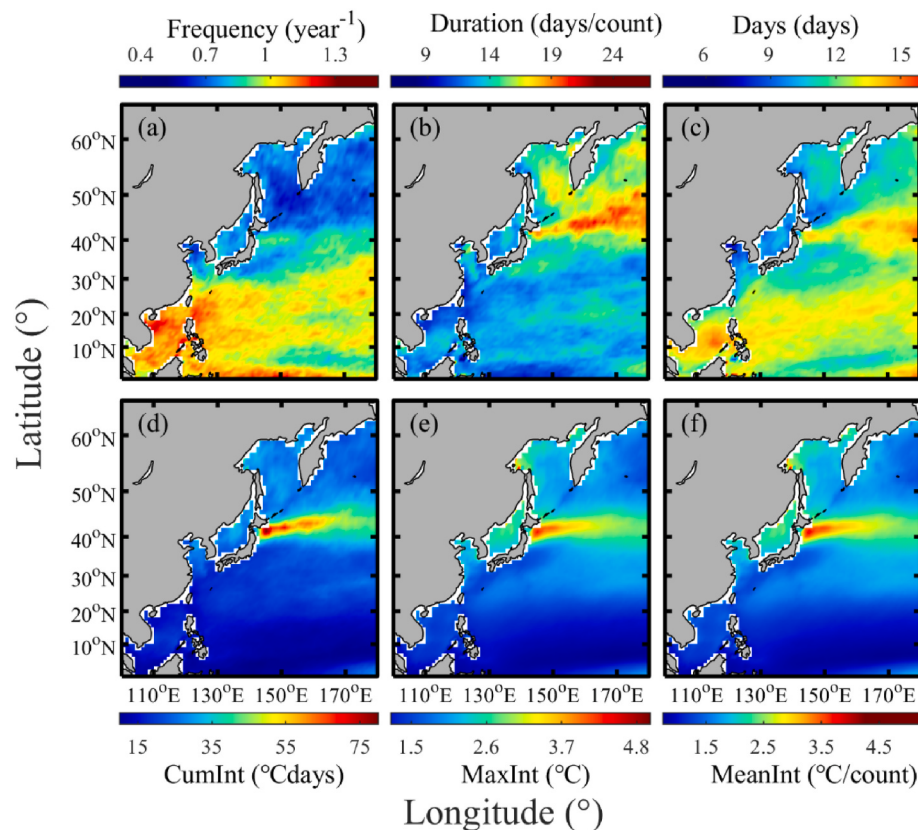


Fig. 6. Spatial distribution of MHWs characteristics in future period (2015–2100) based on the ensemble average of five selected models under the SSP2-4.5. (a ~ f) represent the multi-year averaged MHWs frequency (unit: count/year), duration (unit: days/count), annual cumulative days (Days: unit: days), cumulative intensity (CumInt, unit: °C days), maximum intensity (MaxInt, unit: °C), and mean intensity (MeanInt, unit: °C/count), respectively.

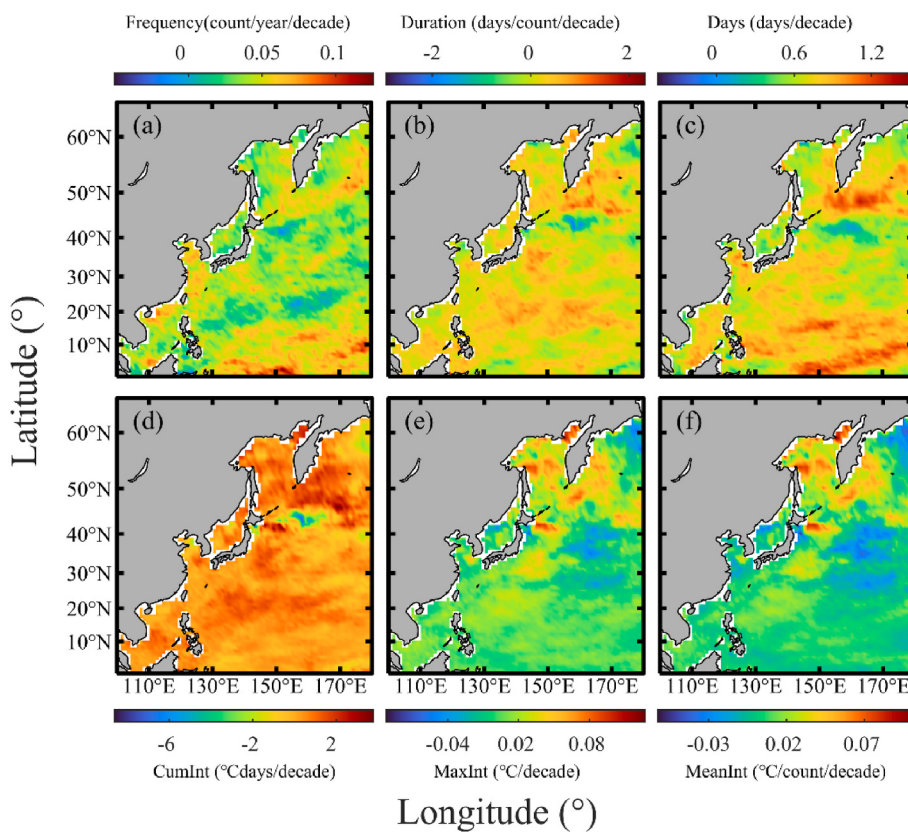


Fig. 7. Spatial distribution of MHWs characteristics trend in the future period (2015–2100) based on the ensemble average of five selected models under the SSP2-4.5 scenario. (a ~ f) represent the trends in MHWs features, including frequency trend (unit: count/year/decade), duration trend (unit: days/count/decade), annual cumulative days trend (unit: days/decade), cumulative intensity trend (unit: °C days/decade), maximum intensity trend (unit: °C/decade), and mean intensity trend (unit: °C/count/decade).

Additionally, the trend shows a slight increase of 0.01 ± 0.02 °C/decade in MHWs' maximum intensity (Fig. 7e) and a slight increase of 0.01 ± 0.01 °C/count/decade in MHWs' average intensity (Fig. 7f). The trends in both the maximum intensity and average intensity are about one-tenth of the results from Yang et al. (2022), which are 0.18 ± 0.08 °C/decade and 0.08 ± 0.03 °C/count/decade, respectively. The most significant trends in the accumulated intensity (3.78 °C days/decade), maximum intensity (0.13 °C/decade), and average intensity (0.10 °C/count/decade) are observed at the points of (169°E, 46°N), (169°E, 61°N), and (169°E, 61°N), respectively. The minimum values for the trends of these three characteristics are -8.62 °C days/decade, -0.09 °C/decade, and -0.06 °C/count/decade, all occurring at the point of (143°E, 42°N).

The SSP5-8.5 scenario represents a future development pathway characterized by high temperature growth and high carbon emissions, with radiative forcing projected to reach 8.5 W/m² by 2100. Under this scenario, the impacts of climate change on the environment and socio-economic systems are significant. Under the SSP5-8.5 scenario, the regions with high multi-year average frequency of MHWs are primarily concentrated in the SCS (Fig. 8a). The high-value regions show a tendency to be more concentrated towards the peripheral maritime areas compared to the SSP2-4.5 scenario. Its average value is 0.84 ± 0.11 count/year, which remains consistent with the results observed in the historical period and the SSP2-4.5 scenario. However, it is significantly lower than the results indicated by Yang et al. (2022). According to the definition employed in this study, there is no significant change in the frequency during the future period. The maximum frequency recorded is 1.26 count/year, observed in the southern waters of Hainan Island at (108°E, 16°N), while the minimum frequency recorded is 0.45 count/year, observed in the equatorial region at (120°E, 0).

The duration of MHWs is notably higher in the open oceans north of

the KE region compared to other areas (Fig. 8b). Under the SSP5-8.5 scenario, the average duration of MHWs is 13.60 ± 1.87 days/count, which is similar to the value observed under the SSP2-4.5 scenario. However, it is significantly lower than the results of 138.66 ± 43.03 days/count obtained in Yang et al. (2022). The maximum duration recorded is 21.07 days/count, observed in the northern part of the KE region at (158°E, 43°N), while the minimum duration is 7.12 days/count, observed at (121°E, 6°N).

There is a longer average annual cumulative days of MHWs in the areas between 20°N and 50°N (Fig. 8c). A particularly prominent high-value region is observed between 40°N and 50°N. The average cumulative days is 11.06 ± 1.37 days/year, slightly lower than the value under the SSP2-4.5 scenario and higher than the value in the historical period. Additionally, it highlights that the average cumulative days are significantly lower than the results reported in Yang et al. (2022), which is presented as 271.59 ± 18.50 days/year. The maximum cumulative days recorded is 15.36 days/year, observed in the north of the KE region at (177°E, 44°N), while the minimum value is 5.43 days/year, observed in the equatorial region at (120°E, 0).

The belt-shaped area between 40°N and 50°N exhibits high multi-year average cumulative intensity, maximum intensity, and average intensity of MHWs (Fig. 8d ~ f). The average cumulative intensity is 22.92 ± 10.28 °C days, slightly higher than the values observed in the SSP2-4.5 scenario and the historical period. However, it remains significantly lower than the results of 385.22 ± 168.00 °C days obtained in Yang et al. (2022). The maximum cumulative intensity recorded is 81.44 °C days, observed in the north of the KE region at (148°E, 42°N), while the minimum cumulative intensity is 6.67 °C days, observed at the point of (125°E, 10°N).

Under the SSP5-8.5 scenario, the average maximum intensity is 1.86 ± 0.64 °C, with a maximum value of 5.44 °C observed at (139°E, 54°N).

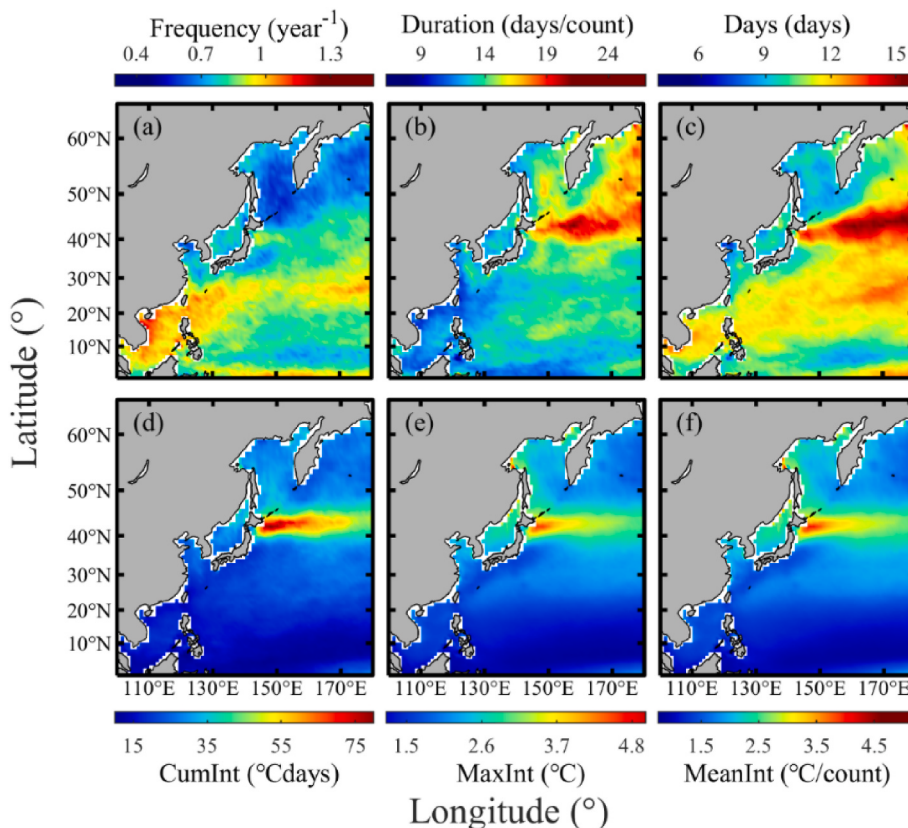


Fig. 8. Spatial distribution of MHWs characteristics in future period (2015–2100) based on the ensemble average of five selected models under the SSP5-8.5 scenario. (a ~ f) represent the multi-year average MHWs frequency (unit: count/year), duration (unit: days/count), annual cumulative days (Days, unit: days), cumulative intensity (CumInt, unit: °C days), maximum intensity (MaxInt, unit: °C), and mean intensity (MeanInt, unit: °C/count), respectively.

The minimum value is $0.70\text{ }^{\circ}\text{C}$ observed at $(120^{\circ}\text{E}, 0)$. This average cumulative intensity is slightly higher than the results observed in the SSP2-4.5 scenario and slightly lower than the values in the historical period and in Yang et al. (2022), although the difference is not significant.

The average intensity of MHWs is $1.63 \pm 0.56\text{ }^{\circ}\text{C}/\text{count}$, with the maximum value reaching $4.63\text{ }^{\circ}\text{C}/\text{count}$ observed at $(139^{\circ}\text{E}, 54^{\circ}\text{N})$. The minimum value is $0.60\text{ }^{\circ}\text{C}/\text{count}$ observed at $(120^{\circ}\text{E}, 0)$. The average value shows no significant differences among the SSP2-4.5 scenario, the historical period, and the results obtained in Yang et al. (2022).

Under the SSP5-8.5 scenario, in the future period (2015–2100), the average trend of MHWs frequency is $0.07 \pm 0.02\text{ count/year/decade}$ (Fig. 9a). This increase rate is approximately twice as high as that under the SSP2-4.5 scenario and one-fifth of the historical period. It is particularly noteworthy that in contrast to the findings of this study, in Yang et al. (2022), this value is negative ($-0.6 \pm 0.1\text{ count/year/decade}$), indicating that the frequency of MHWs will gradually decrease under the SSP5-8.5 scenario. The maximum trend occurs at $(122^{\circ}\text{E}, 18^{\circ}\text{N})$ with a rate of $0.15\text{ count/year/decade}$, while the minimum trend is observed in the north of the KE region at $(140^{\circ}\text{E}, 42^{\circ}\text{N})$ with a value of $-0.03\text{ count/year/decade}$.

The average trend in MHWs duration is $0.17 \pm 0.32\text{ days/count/decade}$ (Fig. 9b). This value is very close to the results obtained under the SSP2-4.5 scenario and is approximately one-third of observed in the historical period. However, it is only one-hundred-and-fiftieth of $25.6 \pm 7.0\text{ days/count/decade}$ indicated by Yang et al. (2022). The maximum trend is observed near the equatorial region at $(122^{\circ}\text{E}, 1^{\circ}\text{N})$ with 1.89 days/decade , while the minimum trend is observed at $(172^{\circ}\text{E}, 45^{\circ}\text{N})$ with -1.30 days/decade .

The average trend in MHWs annual accumulated days is $1.12 \pm 0.27\text{ days/year/decade}$ (Fig. 9c). This value is slightly higher than the results observed under the SSP2-4.5 scenario and approximately half of the value observed in the historical period. However, it is much smaller than the results of $33.8 \pm 2.4\text{ days/year/decade}$ obtained in Yang et al.

(2022). The maximum trend is observed near the equatorial region at $(101^{\circ}\text{E}, 2^{\circ}\text{N})$ with a rate of $2.02\text{ days/year/decade}$, while the minimum trend is observed in the north of the KE region at $(138^{\circ}\text{E}, 54^{\circ}\text{N})$ with a rate of $-0.64\text{ days/year/decade}$.

The trend in accumulated intensity, maximum intensity, and average intensity of MHWs exhibits a relatively consistent pattern in the southern part of the WNP region, with higher values observed north of 40°N . The average trends in these three characteristics of MHWs are $0.68 \pm 0.62\text{ }^{\circ}\text{C days/decade}$, $0.04 \pm 0.03\text{ }^{\circ}\text{C/decade}$, and $0.03 \pm 0.03\text{ }^{\circ}\text{C/count/decade}$, respectively. The average trend in cumulative intensity is approximately twice as high as that under the SSP2-4.5 scenario and shows a similar trend to observed in the historical period. However, it is only one percent of the results of $67.0 \pm 26.1\text{ }^{\circ}\text{C days/decade}$ obtained in Yang et al. (2022). Regarding the maximum intensity and average intensity trends of MHWs, the results under the SSP2-4.5, SSP5-8.5, and Yang et al. (2022) all indicate positive trends. In contrast, the trend in the historical period is negative. Specifically, the trend in maximum intensity (average intensity) under the SSP5-8.5 scenario is approximately four times (three times) that of the SSP2-4.5 scenario and approximately one-eighth (one-third) of the results obtained in Yang et al. (2022). The maximum values for these trends are $4.48\text{ }^{\circ}\text{C days/decade}$, $0.26\text{ }^{\circ}\text{C/decade}$, and $0.22\text{ }^{\circ}\text{C/count/decade}$, observed at points of $(152^{\circ}\text{E}, 41^{\circ}\text{N})$, $(137^{\circ}\text{E}, 55^{\circ}\text{N})$, and $(137^{\circ}\text{E}, 55^{\circ}\text{N})$, respectively. The corresponding minimum values are $-2.79\text{ }^{\circ}\text{C days/decade}$, $-0.07\text{ }^{\circ}\text{C/decade}$, and $-0.07\text{ }^{\circ}\text{C/count/decade}$, observed at points at $(137^{\circ}\text{E}, 37^{\circ}\text{N})$, $(144^{\circ}\text{E}, 41^{\circ}\text{N})$, and $(144^{\circ}\text{E}, 41^{\circ}\text{N})$, respectively.

In terms of the growth rate of MHW frequency, the historical period shows the fastest growth (Fig. 5a), followed by the SSP2-4.5 scenario ($0.02 \pm 0.01\text{ count/decade}$), and the SSP5-8.5 scenario exhibits the slowest growth ($0.008 \pm 0.01\text{ count/decade}$). These trends exhibit a consistent pattern (Fig. 10a), contrary to what was suggested by Yang et al. (2022), where an increase in frequency was projected before 2036 followed by a decrease after that. Regarding the trend in the duration of MHWs, the historical period still demonstrates the fastest change

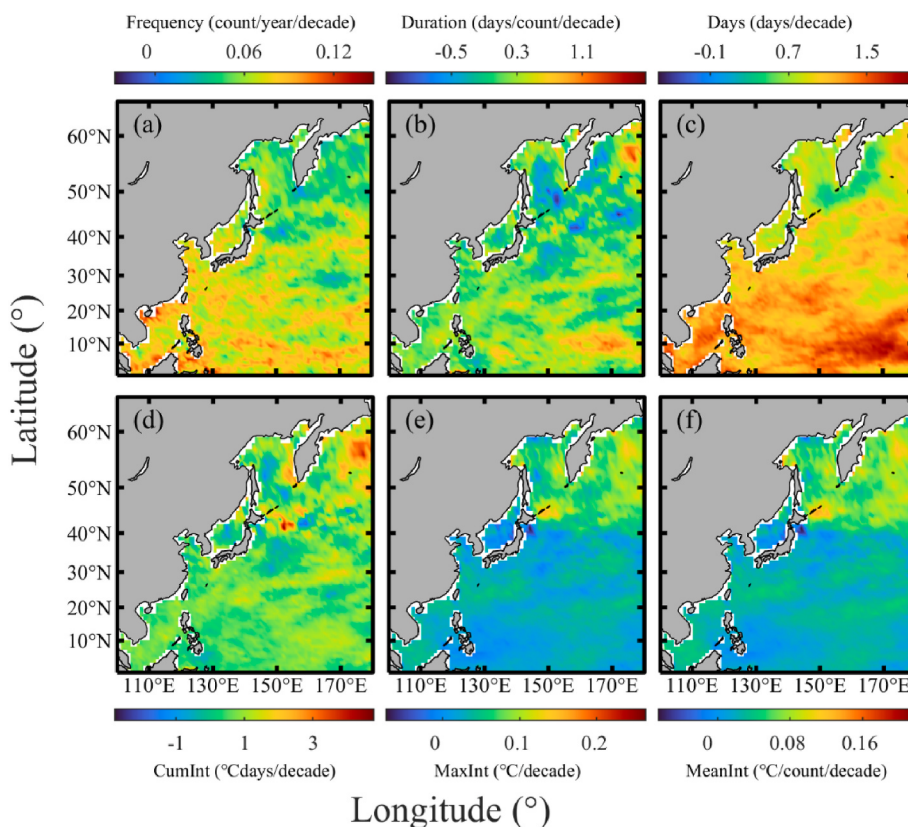


Fig. 9. Spatial distribution of MHWs characteristics trend in the future period (2015–2100) based on the ensemble average of five selected models under the SSP5-8.5 scenario. (a ~ f) represent the trends in MHWs features, including frequency trend (unit: count/year/decade), duration trend (unit: days/count/decade), annual cumulative days trend (unit: days/decade), cumulative intensity trend (unit: $^{\circ}\text{C days/decade}$), maximum intensity trend (unit: $^{\circ}\text{C/decade}$), and mean intensity trend (unit: $^{\circ}\text{C/count/decade}$).

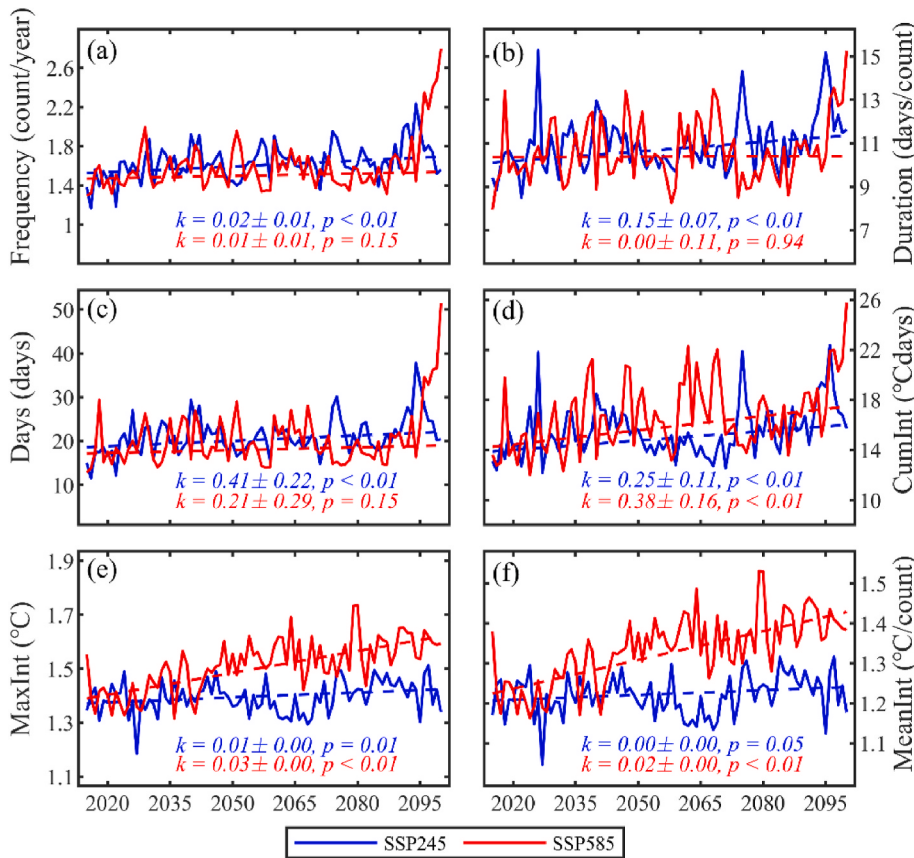


Fig. 10. SSP2-4.5 (blue curve) and SSP5-8.5 (red curve) scenarios, depicting the annual trend in ensemble mean values of MHWs parameters obtained from the selected five models. The solid curve represents the future variation of MHWs parameters, while the dashed line represents the results of linear regression applied to the data. (a ~ f) represent the multi-year average MHWs frequency (unit: count/year), duration (unit: days/count), annual cumulative days (Days, unit: days), cumulative intensity (CumInt, unit: $^{\circ}\text{C}$ days), maximum intensity (MaxInt, unit: $^{\circ}\text{C}$), and mean intensity (MeanInt, unit: $^{\circ}\text{C}/\text{count}$), respectively.

(Fig. 5b), followed by the SSP2-4.5 scenario (0.15 ± 0.07 days/decade), and the SSP5-8.5 scenario (0.004 ± 0.10 days/decade, Fig. 10b). Similarly, since the annual accumulated days of MHWs can be considered as the product of MHW frequency and duration, the order of their changing rates follows the same pattern. The historical period exhibits the fastest increase (Fig. 5c), followed by the SSP2-4.5 scenario (0.40 ± 0.20 days/decade), and then the SSP5-8.5 scenario (0.20 ± 0.30 days/decade, Fig. 10c).

In terms of the trend in cumulative intensity of MHWs, the historical period shows the highest rate of change (Fig. 5d), while under the SSP5-8.5 scenario, there is a faster increase (0.41 ± 0.22 $^{\circ}\text{C}$ days/decade) compared to the SSP2-4.5 scenario (0.30 ± 0.10 $^{\circ}\text{C}$ days/decade, Fig. 10d). The trend in MHW intensity shows a gradual decrease during the historical period (Fig. 5e). However, in both future scenarios, there is an increasing trend (Fig. 10e). Under the SSP2-4.5 scenario, the trend is 0.006 ± 0.005 $^{\circ}\text{C}/\text{decade}$, and under the SSP5-8.5 scenario, it is 0.03 ± 0.004 $^{\circ}\text{C}/\text{decade}$. The trend in average MHW intensity exhibits similar characteristics, with a decreasing trend during the historical period (Fig. 5f). However, in future scenarios, there is an increasing trend (Fig. 10f), with the SSP5-8.5 scenario (0.02 ± 0.004 $^{\circ}\text{C}/\text{decade}$) showing a faster rate of increase compared to the SSP2-4.5 scenario (0.004 ± 0.004 $^{\circ}\text{C}/\text{decade}$).

3.3. Seasonal variations of marine heatwave characteristics

The WNP region is strongly influenced by the East Asian monsoon, and it is currently being studied to understand the occurrence and intensity of MHWs in this area, which are expected to exhibit significant seasonal variations. To investigate the variability of the MHW occurrence area, we define the MHW occurrence area ratio as the ratio of points experiencing MHWs to the total points in the WNP region. The area ratio reflects the product of the cumulative occurrences of MHWs in

the WNP region and their average duration. The calculation results indicate that in future scenarios, the proportion of the MHW occurrence area ratio is significantly higher than that in the historical period (Fig. 11a). Additionally, it is slightly higher in the SSP2-4.5 scenario than in the SSP5-8.5 scenario. In both the historical and future periods, the proportion of the MHW occurrence area ratio is notably higher during autumn (August, September, October) compared to other seasons. In the historical period (SSP2-4.5, SSP5-8.5 scenario), the maximum area ratio is observed in September (August, September), reaching 2.52×10^{-4} (4.12×10^{-4} ; 3.81×10^{-4}), while the minimum value is observed in December (April, January), with only 1.82×10^{-4} (2.91×10^{-4} ; 2.61×10^{-4}).

To further clarify the reasons behind the seasonal variations in the area ratio of MHWs, this study calculates the cumulative occurrences of MHWs in the WNP region during autumn and winter (December, January, February), along with their average durations. The analysis reveals that in the historical period, the SSP2-4.5 scenario, and the SSP5-8.5 scenario, the cumulative occurrences of MHWs in autumn are 951.60 count/year, 1053.83 count/year, and 972.39 count/year, respectively, with corresponding durations of 8.59 days, 12.02 days, and 11.98 days. In contrast, during winter, the cumulative occurrences of MHWs are 716.97 count/year, 598.62 count/year, and 527.76 count/year, with corresponding durations of 9.08 days, 17.86 days, and 17.79 days. It is evident that in these three scenarios, the cumulative occurrences of autumn MHWs are 1.28 times, 1.76 times, and 1.84 times higher than those in winter, while the durations of autumn MHWs are 0.95 times, 0.67 times, and 0.67 times those of winter. Therefore, the higher contribution of autumn MHW occurrences to the area ratio, as compared to winter, is attributed to the greater cumulative occurrences of autumn MHW events. Additionally, the shorter duration of MHWs in autumn, compared to winter, negatively affects the area ratio of MHWs.

The values of the occurrence area ratio obtained in this study are

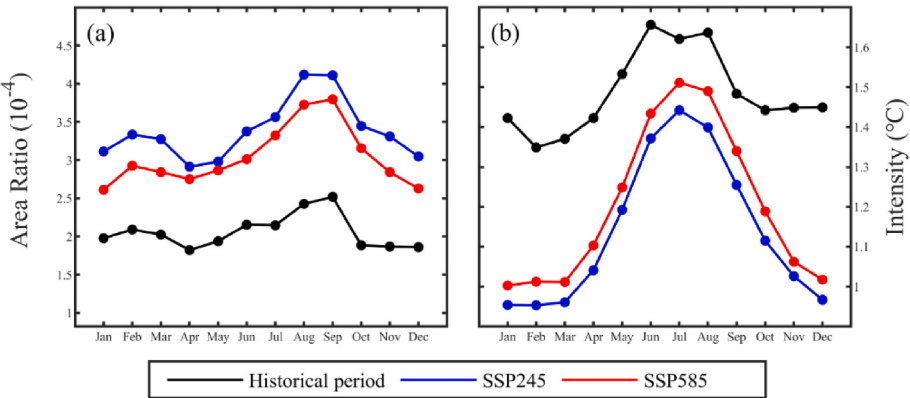


Fig. 11. Monthly distribution of MHWs occurrence area ratio (a) and MHWs average intensity (b) in the WNP region. Black, blue, and red curves represent the distributions in the historical period, SSP2-4.5 and SSP5-8.5 future simulation scenario, respectively.

significantly lower than those reported by Yang et al. (2022). Additionally, the comparison between the historical and future periods in our study shows comparable values, whereas Yang et al. (2022) reports values in the future period that are at least an order of magnitude higher than those in the historical period. The main reason for this discrepancy is likely the use of the sliding climatological threshold method in this study, which reduces the impact of global warming on MHWs. This results in a significant reduction in the differences in MHW characteristics between the historical and future periods.

From the perspective of MHW intensity, both in historical and future scenarios, there is a distinct pattern of stronger MHWs in summer and weaker ones in winter (Fig. 11b). In the historical period, the maximum intensity of MHWs occurs in June (1.66°C), while the minimum intensity occurs in February (1.35°C). Similarly, in the SSP2-4.5 (SSP5-8.5) scenario, the maximum intensity of MHWs occurs in July (July) and reaches 1.44°C (1.51°C), while the minimum intensity occurs in

February (January) and reaches 0.95°C (1.00°C). This seasonal difference pattern is consistent with the findings of Yang et al. (2022), but the magnitudes of the MHW intensity in this study are significantly smaller. Moreover, the most significant difference compared to Yang et al. (2022) is that our findings show lower MHW intensity in the future period compared to the historical period. This suggests that, when employing a sliding climatological threshold, the intensity of future MHWs may not reach the levels reported in previous studies. For a discussion on the seasonal variations contributing to the intensity of MHWs, please refer to the fourth section of this study.

4. Discussion

The variance of SST and the climatic threshold are two critical factors influencing the intensity of MHWs. To further explore the phenomenon observed that the cumulative intensity, maximum intensity, and mean

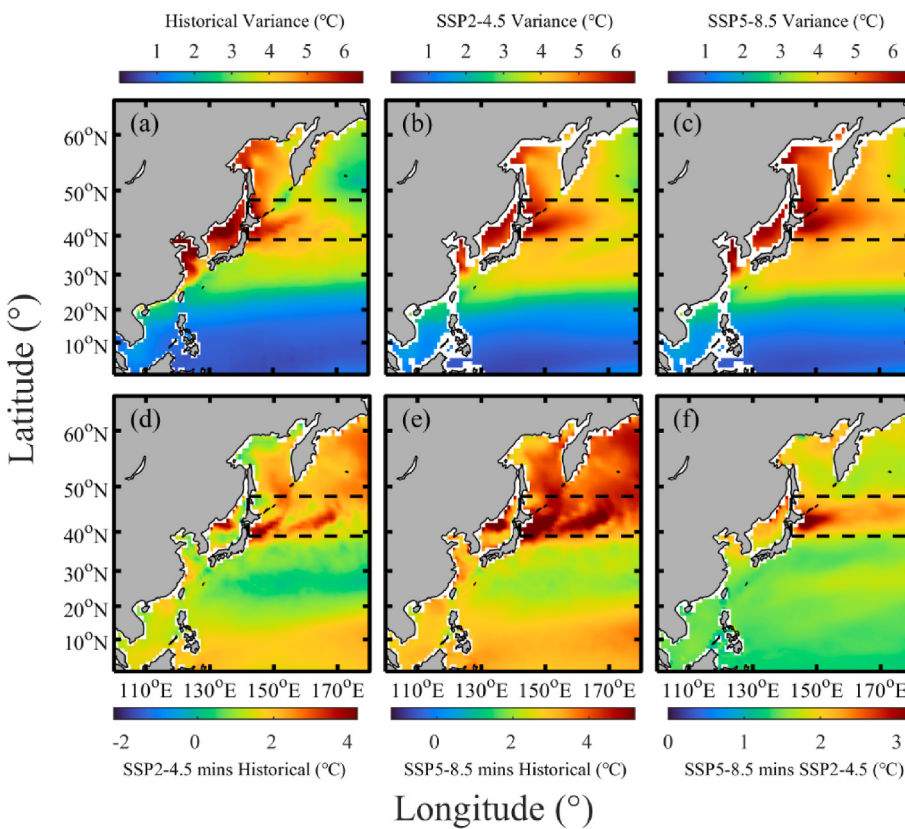


Fig. 12. Spatial distribution of annual sea surface temperature variance and climatological threshold. (a ~ c) sequentially present the sea surface temperature annual variance for three scenarios: historical period (1995–2014), future period under SSP2-4.5 scenario (2081–2100), and future period under SSP5-8.5 scenario (2081–2100). Panels (d ~ f) show the differences in climatological thresholds: between future SSP2-4.5 scenario and historical period, between future SSP5-8.5 scenario and historical period, and between future SSP5-8.5 and SSP2-4.5 scenarios, respectively. The black dashed boxes delineate the Kuroshio Extension and its adjacent area, as indicated in the main text.

intensity of MHWs are significantly higher in the KE and its adjacent waters ($[140^{\circ}\text{E} \sim 180, 38^{\circ}\text{N} \sim 48^{\circ}\text{N}]$, marked by the black dashed box in Fig. 12) compared to other regions, a more detailed analysis is conducted. Fig. 12a ~ c depict the spatial distribution of SST annual variance for the historical period (1995–2014), the future period (2081–2100) under the SSP2-4.5 scenario, and the SSP5-8.5 scenario. It is evident from the figures that the KE and its adjacent waters exhibit the highest SST annual variances. The regional average annual variances are $4.15 \pm 0.75^{\circ}\text{C}$, $4.54 \pm 0.72^{\circ}\text{C}$, and $4.88 \pm 0.65^{\circ}\text{C}$ for these scenarios, whereas outside this region, the average variances are $2.33 \pm 1.63^{\circ}\text{C}$, $2.48 \pm 1.52^{\circ}\text{C}$, and $2.62 \pm 1.62^{\circ}\text{C}$, which is approximately half of the former values. A comparison with Fig. 3d ~ f, 6d ~ f, and 8d ~ f reveals a substantial overlap between the regions with high SST variances in Fig. 12 and the areas characterized by intense cumulative intensity, maximum intensity, and average intensity of MHWs. Therefore, it can be inferred that the pronounced variation in SST, particularly in the KE and its adjacent waters, significantly contributes to the notably higher intensity characteristics of MHWs in this area compared to other regions.

The climatological threshold represents a crucial factor influencing the characteristics of MHWs. The spatial distribution of climatological thresholds is linked to the large-scale SST features, demonstrating a near-uniform pattern in the east-west direction and gradually decreasing from south to north (figure not shown). To clarify spatial differences in climatological thresholds across scenarios, this study presents the differences between the SSP2-4.5 scenario and historical climatological threshold (Fig. 12d), between the SSP5-8.5 scenario and historical climatological threshold (Fig. 12e), and between the SSP5-8.5 and SSP2-4.5 scenarios (Fig. 12f) concerning future climatological thresholds. The most striking observation is the significantly higher values within the KE and its neighboring waters compared to other regions. In Fig. 12d ~ f, the regional average values within the KE and its adjacent waters are $2.12 \pm 0.65^{\circ}\text{C}$, $4.31 \pm 0.82^{\circ}\text{C}$, and $2.19 \pm 0.34^{\circ}\text{C}$, whereas in other regions, corresponding values are merely $1.41 \pm 0.67^{\circ}\text{C}$, $2.96 \pm 0.73^{\circ}\text{C}$, and $1.54 \pm 0.25^{\circ}\text{C}$. This indicates an anticipated substantial SST alteration in the KE and adjacent waters in the future, possibly due to distinct responses to global warming across various WNP subregions. The underlying mechanisms contributing to the divergent responses between the KE area and other regions under the global warming are intriguing. However, delving into this matter exceeds the scope of this study and is a subject for more comprehensive exploration in forthcoming research.

5. Conclusions

MHWs, being catastrophic events, attract widespread attention due to their significant destructive impact on marine ecosystems, as well as various reports documenting their occurrence. Existing research suggests that MHWs have complex mechanisms of formation and exhibit significant variations across different regions. Therefore, the characteristics observed at a global scale may not necessarily apply to specific local regions. Due to its extensive area, the WNP region holds great economic significance for China and neighboring countries, making the study of MHW in this region highly valuable. Firstly, this study provides a detailed analysis of the spatial distribution and temporal trends of six characteristics of MHWs during the historical period. Then, we examines the future trend of MHW characteristics under the SSP2-4.5 and SSP5-8.5 scenarios based on simulated results from five selected models. Thirdly, we investigate the seasonal variations in the occurrence area ratio and intensity of MHWs during both the historical and future periods. The primary conclusions of this study can be summarized as follows.

This study finds that during the historical period, the north area of the WNP region experiences a higher frequency of MHWs, while the occurrence of MHWs in the southern region is relatively lower, with an annual average of less than one event (0.89 ± 0.18 count/year). However, the cumulative intensity, maximum intensity, and average

intensity of MHWs are more evenly distributed without clear high-value regions. During the historical period (1982–2014), the frequency, duration, annual cumulative days, and cumulative intensity of MHWs show a significant increasing trend, with increasing rates of 0.26 ± 0.16 count/decade, 0.45 ± 1.14 days/decade, 2.60 ± 1.62 days/year/decade, and $0.67 \pm 2.88^{\circ}\text{C}$ days/decade, respectively. However, the maximum intensity and average intensity show a slight decreasing trend, with decreasing rates of $-0.02 \pm 0.18^{\circ}\text{C}/\text{decade}$ and $-0.02 \pm 0.14^{\circ}\text{C}/\text{decade}$, respectively.

In the future period (2015–2100), under the SSP2-4.5 scenario, a significant north-south difference in the frequency of MHWs is observed as well. The southern region of the WNP exhibits notably higher MHW frequency compared to the northern region. Most of the WNP region experiences an increasing trend in the frequency of MHWs, with an average value of 0.04 ± 0.02 count/year/decade. The average duration of MHWs is longer in open ocean areas compared to coastal regions, with high-value areas located in the KE region. The cumulative intensity of MHWs also shows an overall increasing trend, with the northern part experiencing a higher increase rate in maximum and average intensities compared to the southern part.

In the SSP5-8.5 scenario, the average MHW frequency is 0.84 ± 0.11 count/year, which is lower than the value in the SSP2-4.5 scenario and slightly lower than the value in the historical period. The average duration of MHWs is 13.60 ± 1.87 days/count, and the average cumulative days is 11.06 ± 1.37 days/year. The KE region exhibits high values for cumulative intensity, maximum intensity, and average intensity. The maximum values for these parameters are 81.44°C days, 5.44°C , and $4.63^{\circ}\text{C}/\text{count}$, respectively.

The average trend of MHWs duration in the SSP5-8.5 scenario is 0.17 ± 0.32 days/count/decade, which is lower than the values observed in the historical period and the SSP2-4.5 scenario. The high-value region for the trend in MHWs cumulative days is observed in the south of the WNP region. Its average value is 1.12 ± 0.27 days/year/decade, which is higher than the values in the SSP2-4.5 scenario but lower than the values in the historical period.

In both the SSP2-4.5 and SSP5-8.5 future scenarios, the occurrence area ratio is significantly larger compared to the historical period, indicating an expansion of the areas affected by MHWs in the future. Specifically, in the SSP2-4.5 scenario, the proportion of the occurrence area is slightly higher than in the SSP5-8.5 scenario. However, the intensity of MHWs is weaker in the SSP2-4.5 scenario compared to the SSP5-8.5 scenario. This suggests that with increasing emissions, MHWs are more likely to occur with higher intensity but in smaller areas.

On a seasonal timescale, both in the historical and future periods, the occurrence area ratio of MHWs is notably higher during autumn compared to other seasons. The exact reasons behind this seasonal difference are still not fully understood. Through separate analysis of the two factors influencing the area ratio of MHWs, it becomes evident that in comparison to the winter, the cumulative occurrence of MHWs is higher during autumn, resulting in an elevated area ratio for this particular season. However, the comparatively shorter duration of MHWs in autumn, as opposed to winter, exerts a detrimental influence on the area ratio. In terms of MHW intensity, regardless of the historical or future scenarios, a consistent pattern emerges with stronger MHWs observed during summer and weaker ones during winter. This seasonal contrast in intensity suggests a distinct seasonality in the occurrence and strength of MHW events.

With the increasing severity of the impacts of MHWs on marine ecosystems and human socio-economic systems, the study of MHWs has become a prominent topic in the field of physical oceanography. The WNP region, known for its dense coastal population and robust economy, hosts numerous nearshore aquaculture zones. Furthermore, the SCS possesses abundant coral reef resources, making it one of the most biodiverse regions. Thus, unveiling the historical and future characteristics of MHWs in the WNP region holds paramount importance. This comprehension not only aids in understanding the hazards posed by

MHWs in this region but also establishes a foundation for future advancements in MHW forecasting systems.

Funding

This study is supported by the National Natural Science Foundation of China under contract No. 42192562; the Open Fund of State Key Laboratory of Satellite Ocean Environment Dynamics, Second Institute of Oceanography, MNR under contract No. QNHN2231; the Innovation Group Project of Southern Marine Science and Engineering Guangdong Laboratory (Zhuhai) under contract No. 311020004; the China Scholarship Council under contract No. 202008320195; Jiangsu Province Higher Education College Students' Innovation and Entrepreneurship Training Program under contract No. 202210300094Y; and the Research Innovation Program for College Graduates of Jiangsu Province under contract No. KYCX23_1350.

Author contributions

WS, LY, YP, CS and YY conceived and designed the experiments. LY, YP and CS performed the experiments. WS, LY, YP, CS and YY analyzed the data. WS, LY, YP, and CS drafted the original manuscript. JJ, JY and CD revised and edited the manuscript.

Declaration of competing interest

The authors declare that they have no known competing financial interests or personal relationships that could have appeared to influence the work reported in this paper.

Data availability

Data will be made available on request.

Acknowledgements

We acknowledge the World Climate Research Programme's (WCRP) Working Group on Coupled Modelling, which is responsible for coordinating CMIP. We also thank the climate modeling groups for producing and making available their model output. We thank Zijie Zhao for providing the main function code to detect marine heatwaves (https://github.com/ZijieZhaoMMHW/m_mhw1.0). We thank the editor and two anonymous reviewers for their constructive comments and helpful suggestions on an earlier version of the manuscript.

References

- Arteaga, L., Rousseaux, C., 2023. Impact of Pacific Ocean heatwaves on phytoplankton community composition. *Commun. Biol.* 6 (1) <https://doi.org/10.1038/s42003-023-04645-0>.
- Belyiana, E., Ningsih, N., Tarya, A., 2022. Characteristics of marine heatwaves (2008–2021) in the savu sea, east nusa tenggara. *J. Phys.: Conf. Ser.* 2377 (1), 12043 <https://doi.org/10.1088/1742-6596/2377/1/012043>.
- Benthuyzen, J., Feng, M., Zhong, L., 2014. Spatial patterns of warming off Western Australia during the 2011 Ningaloo Niño: quantifying impacts of remote and local forcing. *Continent. Shelf Res.* 91, 232–246. <https://doi.org/10.1016/j.csr.2014.09.014>.
- Capotondi, A., Newman, M., Xu, T., et al., 2022. An optimal precursor of Northeast Pacific marine heatwaves and central Pacific El Niño events. *Geophys. Res. Lett.* 49 (5) <https://doi.org/10.1029/2021GL097350> e2021G-e97350G.
- Cavole, L., Demko, A., Diner, R., et al., 2016. Biological impacts of the 2013–2015 warm-water anomaly in the northeast pacific: winners, losers, and the future. *Oceanography* 29 (2), 273–285. <https://doi.org/10.5670/oceanog.2016.32>.
- Chandrapavan, A., Caputi, N., Kangas, M.I., 2019. The decline and recovery of a crab population from an extreme marine heatwave and a changing climate. *Front. Mar. Sci.* 6, 510. <https://doi.org/10.3389/fmars.2019.00510>.
- Chen, W., Jiang, Z., Li, L., 2011. Probabilistic projections of climate change over China under the SRES A1B scenario using 28 AOGCMs. *J. Clim.* 24, 4741–4756. <https://doi.org/10.1175/2011JCLI4102.1>.
- Chen, Z., Shi, J., Liu, Q., et al., 2021. A Persistent and intense marine heatwave in the Northeast Pacific during 2019–2020. *Geophys. Res. Lett.* 48, e2021GL093239 <https://doi.org/10.1029/2021GL093239>.
- Chen, H., Wang, Y., Xiu, P., et al., 2023. Combined oceanic and atmospheric forcing of the 2013/14 marine heatwave in the northeast Pacific. *npj Climate and Atmospheric Science* 6, 3. <https://doi.org/10.1038/s41612-023-00327-0>.
- Chiswell, S.M., 2022. Global trends in marine heatwaves and cold spells: the impacts of fixed versus changing baselines. *J. Geophys. Res.* 127, e2022JC018757 <https://doi.org/10.1029/2022JC018757>.
- Doni, L., Oliveri, C., Lasa, A., et al., 2023. Large-scale impact of the 2016 marine heatwave on the plankton-associated microbial communities of the Great Barrier Reef (Australia). *Mar. Pollut. Bull.* 188, 114685 <https://doi.org/10.1016/j.marpolbul.2023.114685>.
- Elzahaby, Y., Schaeffer, A., Roughan, M., et al., 2021. Oceanic circulation drives the deepest and longest marine heatwaves in the East Australian Current system. *Geophys. Res. Lett.* 48, e2021GL094785 <https://doi.org/10.1029/2021GL094785>.
- Eyring, V., Bony, S., Meehl, G.A., et al., 2016. Overview of the coupled model intercomparison project phase 6 (CMIP6) experimental design and organization. *Geosci. Model Dev. (GMD)* 9, 1937–1958. <https://doi.org/10.5194/gmd-9-1937-2016>.
- Frölicher, T.L., Fischer, E.M., Gruber, N., 2018. Marine heatwaves under global warming. *Nature* 560 (7718), 360–364. <https://doi.org/10.1038/s41586-018-0383-9>.
- Gao, G., Marin, M., Feng, M., et al., 2020. Drivers of marine heatwaves in the East China sea and the South yellow Sea in three consecutive summers during 2016–2018. *J. Geophys. Res.* 125 (8) <https://doi.org/10.1029/2020JC016518> e2020J-e16518J.
- Garrabou, J., Gómez-Gras, D., Medrano, A., et al., 2022. Marine heatwaves drive recurrent mass mortalities in the Mediterranean Sea. *Global Change Biol.* 28, 5708–5725. <https://doi.org/10.1111/gcb.16301>.
- Gawarkiewicz, G., Chen, K., Forsyth, J., et al., 2019. Characteristics of an advective marine heatwave in the Middle Atlantic Bight in early 2017. *Front. Mar. Sci.* 6, 712. <https://doi.org/10.3389/fmars.2019.00712>.
- Hayashida, H., Matear, R., Strutton, P., et al., 2020. Insights into projected changes in marine heatwaves from a high-resolution ocean circulation model. *Nat. Commun.* 11, 4352. <https://doi.org/10.1038/s41467-020-18241-x>.
- Hobday, A.J., Alexander, L.V., Perkins, S.E., et al., 2016. A hierarchical approach to defining marine heatwaves. *Prog. Oceanogr.* 141, 227–238. <https://doi.org/10.1016/j.pocean.2015.12.014>.
- Holbrook, N.J., Coauthors, 2019. A global assessment of marine heatwaves and their drivers. *Nat. Commun.* 10 (1), 2624. <https://doi.org/10.1038/s41467-019-10206-z>.
- Jacox, M.G., Tommasi, D., Alexander, M.A., et al., 2019. Predicting the evolution of the 2014–2016 California Current System marine heatwave from an ensemble of coupled global climate forecasts. *Front. Mar. Sci.* 6, 497. <https://doi.org/10.3389/fmars.2019.00497>.
- Jacox, M.G., Alexander, M.A., Amaya, D., et al., 2022. Global seasonal forecasts of marine heatwaves. *Nature* 604 (7906), 486–490. <https://doi.org/10.1038/s41586-022-04573-9>.
- Kajtar, J.B., Hernaman, V., Holbrook, N.J., et al., 2022. Tropical western and central pacific marine heatwave data calculated from gridded sea surface temperature observations and CMIP6. *Data Brief* 40, 107694. <https://doi.org/10.1016/j.dib.2021.107694>.
- Laufkötter, C., Zscheischler, J., Frölicher, T.L., 2020. High impact marine heatwaves attributable to human-induced global warming. *Science* 369 (6511), 1621–1625.
- Le, G.N., Zscheischler, J., Rodgers, K.B., et al., 2022. Hotspots and drivers of compound marine heatwaves and low net primary production extremes. *Biogeosciences* 19, 5807–5835. <https://doi.org/10.5194/bg-19-5807-2022>.
- Li, D., Chen, Y., Qi, J., et al., 2023. Attribution of the July 2021 record-breaking Northwest Pacific marine heatwave to global warming, atmospheric circulation, and ENSO. *Bull. Am. Meteorol. Soc.* 104, E291–E297. <https://doi.org/10.1175/BAMS-D-22-0142.1>.
- Liu, Y., Dong, C., Guan, Y., et al., 2012. Eddy analysis in the subtropical zonal band of the North Pacific Ocean. *Deep Sea Res.* 68, 54–67. <https://doi.org/10.1016/j.dsr.2012.06.001>.
- Liu, G., Heron, S.F., Eakin, C.M., et al., 2014. Reef-scale thermal stress monitoring of coral ecosystems: new 5-km global products from NOAA coral reef watch. *Rem. Sens.* 6 (11), 11579–11606. <https://doi.org/10.3390/rs61111579>.
- Liu, K., Xu, K., Zhu, C., et al., 2022. Diversity of marine heatwaves in the South China Sea regulated by ENSO phase. *J. Clim.* 35, 877–893. <https://doi.org/10.1175/JCLI-D-21-0309.1>.
- Mills, K., Pershing, A., Brown, C., et al., 2013. Fisheries management in a changing climate: lessons from the 2012 ocean heatwave in the northwest Atlantic. *Oceanography* 26 (2), 191–195. <https://doi.org/10.5670/oceanog.2013.27>.
- Noh, K., Lim, H., Kug, J.S., 2022. Global chlorophyll responses to marine heatwaves in satellite ocean color. *Environ. Res. Lett.* 17 (6), 64034 <https://doi.org/10.1088/1748-9326/ac70ec>.
- O'Neill, B.C., Tebaldi, C., van Vuuren, D.P., et al., 2016. The scenario model intercomparison project (Scenario MIP) for CMIP6. *Geosci. Model Dev. (GMD)* 9 (9), 3461–3482. <https://doi.org/10.5194/gmd-9-3461-2016>.
- Oh, H., Kim, G., Kim, Y.S., et al., 2023. Classification and causes of East Asian marine heatwaves during boreal summer. *J. Clim.* 36, 1435–1449. <https://doi.org/10.1175/JCLI-D-22-0369.1>.
- Oliver, E.C.J., Benthuyzen, J., Bindoff, N., et al., 2017. The unprecedented 2015/16 Tasman Sea marine heatwave. *Nat. Commun.* 8, 16101 <https://doi.org/10.1038/ncomms16101>.
- Oliver, E.C.J., Donat, M.G., Burrows, M.T., et al., 2018. Longer and more frequent marine heatwaves over the past century. *Nat. Commun.* 9, 1324. <https://doi.org/10.1038/s41467-018-03732-9>.
- Oliver, E.C.J., Burrows, M.T., Donat, M.G., et al., 2019. Projected marine heatwaves in the 21st century and the potential for ecological impact. *Front. Mar. Sci.* 6, 734. <https://doi.org/10.3389/fmars.2019.00734>.

- Oliver, E.C.J., Jessica, A., Benthuysen, S., et al., 2020. Marine heatwaves. *Ann. Rev. Mar. Sci.* 13, 313–342. <https://doi.org/10.1146/annurev-marine-032720-095144>.
- Pearce, A.F., Feng, M., 2013. The rise and fall of the “marine heat wave” off Western Australia during the summer of 2010/2011. *J. Mar. Syst.* 111–112, 139–156.
- Plecha, S.M., Soares, P.M.M., 2020. Global marine heatwave events using the new CMIP6 multi-model ensemble: from shortcomings in present climate to future projections. *Environ. Res.* 15 (12), 124058.
- Plecha, S., Soares, P.M.M., Silva, S., et al., 2021. On the uncertainty of future projections of marine heatwave events in the North Atlantic Ocean. *Clim. Dynam.* 56 <https://doi.org/10.1007/s00382-020-05529-3>.
- Qiu, Z., Qiao, F., Jang, C., et al., 2021. Evaluation and projection of global marine heatwaves based on CMIP6 models. *Deep Sea Res.* 194, 104998 <https://doi.org/10.1016/j.dsr2.2021.104998>.
- Reynolds, R.W., Smith, T.M., Liu, C., et al., 2007. Daily high-resolution-blended analyses for sea surface temperature. *J. Clim.* 20 (22), 5473–5496. <https://doi.org/10.1175/2007JCLI1824.1>.
- Rodrigues, R.R., Taschetto, A.S., Gupta, A.S., et al., 2019. Common cause for severe droughts in South America and marine heatwaves in the South Atlantic. *Nat. Geosci.* 12, 620–626. <https://doi.org/10.1038/s41561-019-0393-8>.
- Scafetta, N., 2022. CMIP6 GCM ensemble members versus global surface temperatures. *Clim. Dynam.* 60 (9–10), 1–30. <https://doi.org/10.1007/s00382-022-06493-w>.
- Sen, G.A., Thomsen, M., Benthuysen, J.A., et al., 2020. Drivers and impacts of the most extreme marine heatwave events. *Sci. Rep.* 10, 19359 <https://doi.org/10.1038/s41598-020-75445-3>.
- Smith, K., Burrows, M., Hobday, A., et al., 2021. Socioeconomic impacts of marine heatwaves: global issues and opportunities. *Science* 374 (6566). <https://doi.org/10.1126/science.abj3593>.
- Smith, K.E., Burrows, M.T., Hobday, A.J., et al., 2023. Biological impacts of marine heatwaves. *Ann. Rev. Mar. Sci.* 15, 119–145. <https://doi.org/10.1146/annurev-marine-032122-121437>.
- Sun, W., An, M., Liu, J., et al., 2022b. Comparative analysis of four types of mesoscale eddies in the Kuroshio-Oyashio extension region. *Front. Mar. Sci.* 9 <https://doi.org/10.3389/fmars.2022.984244>.
- Sun, D., Jing, Z., Li, F., et al., 2022a. Characterizing global marine heatwaves under a spatio-temporal framework. *Prog. Oceanogr.* 211, 102947 <https://doi.org/10.1016/j.pocean.2022.102947>.
- Szymkowiak, M., Steinkruger, A., 2023. Alaska Fishers attest to climate change impacts in discourse on resource management under marine heatwaves. *Environ. Sci. Pol.* 140, 261–270. <https://doi.org/10.1016/j.envsci.2022.12.019>.
- Wang, Q., Zhang, B., Zeng, L., et al., 2022a. Properties and drivers of marine heat waves in the Northern South China Sea. *J. Phys. Oceanogr.* 52, 917–927. <https://doi.org/10.1175/JPO-D-21-0236.1>.
- Wang, D., Xu, T., Fang, G., et al., 2022b. Characteristics of marine heatwaves in the Japan/East Sea. *Rem. Sens.* 14 (4), 936. <https://doi.org/10.3390/rs14040936>.
- Taylor, K.E., 2001. Summarizing multiple aspects of model performance in a single diagram. *J. Geophys. Res.: Atmosph.* 106, 7183–7192. <https://doi.org/10.1029/2000JD900719>.
- Wang, S., Jing, Z., Wu, L., et al., 2023a. Southern hemisphere eastern boundary upwelling systems emerging as future marine heatwave hotspots under greenhouse warming. *Nat. Commun.* 14 (1) <https://doi.org/10.1038/s41467-022-35666-8>.
- Wang, Y., Zhang, C., Tian, S., et al., 2023b. Seasonal cycle of marine heatwaves in the northern South China Sea. *Clim. Dynam.* 1–11 <https://doi.org/10.1007/s00382-023-06747-1>.
- Wei, M., Shu, Q., Song, Z., et al., 2021. Could CMIP6 climate models reproduce the early-2000s global warming slowdown? *Sci. China Earth Sci.* 64, 853–865. <https://doi.org/10.1007/s11430-020-9740-3>.
- Wernberg, T., Smale, D.A., Tuya, F., et al., 2013. An extreme climatic event alters marine ecosystem structure in a global biodiversity hotspot. *Nat. Clim. Change* 3 (1), 78–82. <https://doi.org/10.1038/nclimate1627>.
- Yan, Y., Chai, F., Xue, H., et al., 2020. Record-breaking sea surface temperatures in the yellow and East China Seas. *J. Geophys. Res.* 125, e2019JC015883 <https://doi.org/10.1029/2019JC015883>.
- Yang, Y., Sun, W., Yang, J., et al., 2022. Analysis and prediction of marine heatwaves in the Western North Pacific and Chinese coastal region. *Front. Mar. Sci.* 9, 1048557 <https://doi.org/10.3389/fmars.2022.1048557>.
- Yao, Y., Wang, C., 2021. Variations in summer marine heatwaves in the South China Sea. *J. Geophys. Res.* 126, e2021JC017792 <https://doi.org/10.1029/2021JC017792>.
- Yao, Y., Wang, C., 2022. Marine heatwaves and cold-spells in global coral reef zones. *Prog. Oceanogr.* 209, 102920 <https://doi.org/10.1016/j.pocean.2022.102920>.
- Yao, Y., Wang, C., Wang, C., 2023. Record-breaking 2020 summer marine heatwaves in the western North Pacific. *Deep Sea Res.* 209, 105288 <https://doi.org/10.1016/j.dsr2.2023.105288>.
- Zhang, X., Zheng, F., Zhu, J., et al., 2022. Observed frequent occurrences of marine heatwaves in most ocean regions during the last two decades. *Adv. Atmos. Sci.* 39 (9), 1579–1587. <https://doi.org/10.11922/sciedb.00872>.